NASA CR-72508
Allison EDR 5923

43
N69-19022

DESIGN OF A STRUT SUPPORTED TURBINE VANE WITH A WIRE-FORM POROUS SHELL

by

D. A. Nealy and R. D. Anderson

ALLISON DIVISION OF GENERAL MOTORS

prepared for

NATIONAL AERONAUTICS AND SPACE ADMINISTRATION

NASA Lewis Research Center
Contract NAS3-7913
Edward Warren, Project Manager
Robert Hickel, Research Advisor

NOTICE

NASA CR-72508
Allison EDR 5923

PERIODIC REPORT

DESIGN OF A STRUT SUPPORTED TURBINE VANE WITH A WIRE-FORM POROUS SHELL

by

D. A. Nealy and R. D. Anderson

ALLISON DIVISION OF GENERAL MOTORS
Indianapolis, Indiana

prepared for

NATIONAL AERONAUTICS AND SPACE ADMINISTRATION

15 July 1968

CONTRACT NAS3-7913

NASA Lewis Research Center
Cleveland, Ohio
Edward Warren, Project Manager
Robert Hickel, Research Advisor
Airbreathing Engines Division

FOREWORD

The work described herein was conducted by the Heat Transfer Section, Engineering Sciences Department, Allison Division of General Motors, under NASA Contract NAS3-7913. The work was done under the management of the NASA Project Manager, Mr. Edward L. Warren, Airbreathing Engines Division, NASA-Lewis Research Center. Mr. H. E. Helms served as the Allison Project Manager.

The authors wish to acknowledge the support given this study by Messrs R. O. Hickel, H. H. Ellerbrock, and J. N. B. Livingood of the Airbreathing Engines Division, NASA-Lewis Research Center.

TABLE OF CONTENTS

Page

Summary. 1

Introduction 2

General Description of Design 5

Design Conditions 7
  On-Design Conditions 7
  Off-Design Conditions 8

Thermal Analysis 9
  General Approach 9
  Determination of Ideal Injection Distribution 10
  Determination of Compartment Design 11
  Method of Skin Temperature Analysis 12
  Method of Strut Temperature Analysis 16
  Numerical Results and Discussion 18

Stress Analysis 23
  Skin Deflection Calculation 23
  Vane Strut Stress Analysis 23

Appendix A—List of Symbols 25

Appendix B—Heat Transfer Analysis for Transpiration
  Cooled Walls 29

References 39

LIST OF TABLES

Table	Title	Page
I	Design condition cavity pressures and orifice areas.	41
II	Tabulated values of skin temperatures for the design condition	42
III	Strut temperature pattern at the mean section for the design condition	48
IV	Off-design cavity pressures and flow rates	49
V	Tabulated values of skin temperatures for the off-design condition	50
VI	Strut temperature pattern at the mean section for the off-design condition	56
VII	Tabulation of F_1 function	57
VIII	Tabulation of F_2 function	58

LIST OF ILLUSTRATIONS

Figure	Title	Page
1	Poroloy vane and strut mean section	59
2	Airfoil coordinates	60
3a	Vane construction details and strut coordinates (side view)	61
3b	Vane construction details (hub section view)	62
3c	Vane construction details (mean and tip section views)	63
3d	Vane construction details (side view)	64
3e	Vane construction details (side view)	65
3f	Vane construction details (top view)	66
4	Gas-stream velocity distributions for the design condition	67
5	Gas-stream static pressure distributions for the design condition	68
6	Gas-stream static temperature distributions for the design condition	69
7	Gas-stream temperature distribution at stator inlet	70
8a	Comparison of actual and ideal blowing distributions for hub section at the design condition	71
8b	Comparison of actual and ideal blowing distributions for mean section at the design condition	72
8c	Comparison of actual and ideal blowing distributions for tip section at the design condition	73
9	Schematic diagram of unfolded airfoil	74
10	Typical node pattern	74
11	Strut simulation for numerical conduction analysis	75
12	Nodal network for Poroloy skin thermal analysis	76
13	Poroloy vane isotherm map for the design condition	77
14	Isotherm pattern for strut meanline section at the design condition	78
15a	Predicted blowing distribution for hub section at the off-design condition	79
15b	Predicted blowing distribution for mean section at the off-design condition	80
15c	Predicted blowing distribution for tip section at the off-design condition	81
16	Poroloy vane isotherm map for off-design condition	82
17	Basic physical model	83

ABSTRACT

Details of the thermal and structural design analysis of a strut supported, porous wall turbine vane are presented. Calculations are made relative to the determination of required injection rate distributions, which in turn establish the internal compartmentation design and flow passage sizing. Calculated porous skin and strut cross section temperature distributions are presented for both design and off-design conditions. A simple structural analysis is performed to determine the stress levels in the strut and porous shell caused by gas and coolant pressure distributions around the airfoil. The calculated results show that the proposed design will exhibit satisfactory performance at the design condition.

DESIGN OF A STRUT SUPPORTED TURBINE VANE WITH A WIRE-FORM POROUS SHELL

by

D. A. Nealy and R. D. Anderson

Allison Division, General Motors

SUMMARY

An analytical study of the temperature distribution in the strut and shell of a strut supported transpiration cooled turbine vane was made for a design condition consisting of a combustion gas total temperature of 2500°F, a combustion gas total pressure of 42 psia, and a cooling air temperature of 1200°F. The design incorporated a constant permeability porous shell. The core region of the airfoil was compartmented and an orifice in the base region of each compartment provided metering of the coolant in an attempt to maintain a uniform shell temperature. The design objective was to strive for a reasonably constant porous shell temperature distribution within practical limitations. The maximum shell temperature for the design conditions was limited to the order of 1700°F. The shell and strut temperatures were also determined for an off-design combustion gas condition (total temperature of 2500°F, total pressure of 105 psia) after the shell permeability and orifice sizes had been fixed for the design conditions. A simple stress analysis was made to determine the stresses in the strut and porous shell caused by the combustion gas pressure distributions around the vane airfoil. The results indicated that for the design conditions a suitable porous wall temperature ranging from a maximum local temperature of about 1740°F to a minimum of 1382°F was obtained; the average shell temperature was about 1560°F. The associated coolant-to-gas flow ratio was about 0. 053 and the required cooling air pressure at the vane inlet was about 52 psia. For the off-design condition, the local shell temperatures ranged from a maximum of 1882°F to a minimum of 1327°F; the average shell temperature remained about the same as for the design condition. The average strut temperature was about 100°F higher for the off-design condition than for the design condition. The coolant-to-gas flow ratio was about 0. 049 and the required cooling air pressure at the vane inlet was about 115 psia. The shell and strut stress conditions were within suitable limits for the gas pressure loading conditions.

INTRODUCTION

This investigation was made as part of an overall study of turbine cooling that is being conducted by the Lewis Research Center of the National Aeronautics and Space Administration. A portion of the overall program of the Lewis Research Center is directed toward the development of oxidation resistant wire-form porous materials that should provide greater resistance to internal oxidation and clogging than do the currently available wire-form materials. This program is expected to provide the Lewis Research Center with oxidation resistant wire-form porous material that can be used in the fabrication of vanes or blades for research purposes. The study reported herein was conducted as part of a contract to provide the Lewis Research Center with the detail design of a transpiration cooled wire-form vane that could be fabricated and subsequently tested in a particular Lewis Research Center static cascade or engine facility.

The study reported herein involved the thermal design of a strut supported, transpiration cooled turbine vane and represents a portion of the work that was conducted under Contract No. NAS3-7913. A limited structural analysis of the vane was also performed, primarily relating to gas pressure loads on the strut and airfoil skin. The Lewis Research Center specified the airfoil size, the airfoil outer contour, and the "design" and "off-design" operating conditions under which it was anticipated that the vane might be tested. It was further specified that the vane design was to use Poroloy (a wire-form porous material produced by the Bendix Corporation) as the porous airfoil shell.

The specified design conditions were a combustion gas total temperature of 2500°F, a combustion gas total pressure of 42 psia, and a cooling air total temperature of 1200°F. These design conditions were selected because they represent the maximum temperature and pressure conditions of a research engine facility that the Lewis Research Center has for air-cooled vane testing purposes. It was further specified that the porous shell was to have a constant permeability. The design objective was to strive for a reasonably constant porous shell temperature distribution within practical limitations. To accomplish this objective, the core region of the airfoil was compartmented and an orifice in the base region of each compartment was provided to meter the coolant in an attempt to achieve a reasonably uniform shell temperature. After the shell permeability, compartment geometry, and orifice sizes were determined and fixed for the design condition, a thermal analysis of the vane was made for an off-design combustion gas condition. The off-design gas conditions were a total temperature of 2500°F and a total pressure of 105 psia. These conditions were selected because they represent the projected conditions that may be available to the Lewis Research Center test facility at some future date.

The thermal analysis made herein determined the local temperature distributions in the porous shell and in the supporting strut. The analysis presented is based largely on a method developed recently in a doctoral thesis and is discussed in detail in Reference 1. The actual calculations were made by employing existing Allison Division computer programs developed for an IBM 360-44 computer system.

A simple stress analysis was also made to determine the effects of the combustion gas pressures on the deflections and resulting stresses in the porous shell and the supporting strut.

GENERAL DESCRIPTION OF DESIGN

The general arrangement of the strut cross section supported vane is shown in Figure 1. Additional information relating to airfoil coordinates, strut dimensions, base orifice sizes, etc is presented in Figures 2 and 3.

The design is basically a strut supported, constant permeability porous wall airfoil. The strut and end attachments are an integral casting of Udimet 700. The strut essentially carries the gas bending loads on the airfoil and provides compartments within the interior of the airfoil to properly distribute cooling air through the constant permeability airfoil skin. The pressures in each compartment are controlled by orifices drilled in the base of the strut casting (Figure 3f). There are ten lands or attachment regions on the strut, each land being approximately 0.100 in. wide. The strut is attached to the skin at each attachment region with a continuous spanwise electron beam weld. The attachment of the strut to the skin defines ten individual internal compartments. However, compartments D and E (Figure 1) are supplied at a common plenum pressure, with air passages cast through the strut dividing these two compartments. The primary purpose of the strut in this region was to stiffen the porous wall against excessive deflection caused by outward gas pressure forces. Compartments I and J are also supplied at a common plenum pressure; therefore, the strut and land between these compartments serve only to stiffen the wall of the porous airfoil skin.

The strut design was guided primarily by considerations related to ease of casting and efficient heat transfer. The relatively thick land sections aid in the efficient transfer of heat from the weld regions to the coolant channels. In addition, the wide land sections were necessary to obtain a reliable electron beam weld of the skin to the strut. The coolant channels were also made as large as possible in cross section to reduce pressure loss in the spanwise direction in the compartments. Load carrying characteristics were also considered, but were of secondary importance because of the vane application. Stress analysis of the strut relative to gas bending loads showed that it would operate well within allowable stress limits at the design condition (Stress Analysis section).

The airfoil coordinates shown in Figure 2 correspond to the first-stage vane of a modified Pratt & Whitney J-75 engine currently being used as an experimental heat transfer engine by the Lewis Research Center. In this design, the airfoil skin (Poroloy) was considered to be a wire-wound porous material manufactured by the Bendix Corporation. Specifically, the design is based on a Poroloy skin made of TD Ni-Cr alloy, having a constant permeability (flow resistance) which corresponds to an index of 2×10^{-11} as shown in Figure P. No. 039270 of Reference 2. This permeability level was chosen primarily to satisfy the relatively large leading edge injection requirement without incurring an excessive pressure drop. The porous skin thickness was considered to be constant and was assumed to be about 0.0245 in.

Poroloy made of materials other than TD Ni-Cr could be used in the present design provided the differences in thermal and physical properties receive proper consideration. A more complete description of the Poroloy material and its manufacture is presented in Reference 2.

DESIGN CONDITIONS

ON-DESIGN CONDITIONS

The primary design conditions which governed the design of the subject turbine vane were based on anticipated operating conditions of the static cascade facility in which the vane is to be tested. These conditions are:

Combustion gas-stream total temperature	2500°F (nominal)
Combustion gas-stream total pressure	42 psia (flat profile)
Cooling air supply temperature	1200°F
Cooling air supply pressure	44 psia*
Desired maximum porous skin temperature	1700°F

The distributions of gas-stream (free-stream) velocity, static pressure, and static temperature around the airfoil for the design conditions are shown in Figures 4, 5, and 6. These distributions are based on a potential flow analysis of the combustion gas in the cascade vane channels. This analysis provides prediction of suction and pressure side stream Mach number distributions which correspond to the corrected flow rate through the cascade. The physical velocity, temperature, and pressure distributions can then be obtained using conventional isentropic flow relationships. The potential flow prediction technique is conventional in all respects and is discussed in Reference 3. The gas-stream total temperature profile (spanwise) is shown in Figure 7 and represents the anticipated maximum vane inlet total temperature that might be encountered in the Lewis-Research Center engine test facility.

The desired maximum vane skin temperature of 1700°F is based primarily on criteria related to a reasonable oxidation life for static cascade testing. Because of the vane application and the use of a supporting strut, it was felt that oxidation life requirements were more critical than life requirements based on strength considerations—e.g., stress-rupture life. Limited strength and oxidation data for the Poroloy material are presented in Reference 4.

---

* Revised to 52 psia following design calculations.

OFF-DESIGN CONDITIONS

The anticipated off-design conditions are:

Combustion gas-stream total temperature	2500°F (nominal)
Combustion gas-stream total pressure	105 psia (flat profile)
Cooling air supply temperature	1200°F
Cooling air supply pressure	115 psia

The only change from the design conditions in this case is the increase in gas-stream total pressure. Since the cascade corrected flow, vane profile, and vane setting angle will be unchanged, the velocity and static pressure distributions shown in Figures 4 and 6 remain the same. The distribution of gas-stream static pressures is the same as shown in Figure 5, except that all local static pressure values are increased by a factor of 2.5 (105/42). The gas-stream total temperature profile (spanwise) at the vane inlet is assumed to be the same as that for the design condition (Figure 7).

THERMAL ANALYSIS

GENERAL APPROACH

The primary objective of the thermal analysis was to establish a strut-compartmented vane design which would satisfy as nearly as possible the desired isothermal skin temperature condition, neglecting end effects. After a given design was established, it was necessary to perform a detailed thermal analysis of the entire strut-skin design to predict the skin temperature distributions which would be expected in practice. The latter analysis included those areas of the skin that were attached (welded) to the strut, and reflected the conduction heat flow into the strut at the attachment points.

The first step of the analysis involved the determination of the injection distribution which would satisfy the isothermal skin temperature condition. This injection distribution reflects the thermal boundary layer development over the exterior airfoil surface and is commonly called the ideal injection distribution. The compartment design and pressures were then established to best simulate the ideal injection distribution. Since the ideal injection distribution is rarely achieved in practice, the final analysis of the strut-skin design must reflect nonisothermal surface effects on boundary layer development as well as wall conduction effects.

The analysis which was applied to this problem is capable of treating the two-dimensional conduction heat flow in the skin (spanwise and chordwise). In addition, the two-dimensional temperature pattern in the strut was also determined through a section taken at midspan. Because the heat flow into the strut is introduced at the welded strut-skin interfaces (Figure 1), the skin and strut heat transfer problems are necessarily coupled. However, since the conduction heat flows in the skin and strut are in two different planes, the overall problem is three-dimensional. No single analytical technique is presently capable of treating the coupled three-dimensional problem; therefore, two existing analyses were applied in an iterative manner to obtain a satisfactory solution. The essential steps of this approach, which will be described later, were as follows.

1. The ideal injection distribution was determined for the design conditions based on a constant (isothermal) skin temperature of 1700°F.

2. The skin permeability level was chosen to satisfy the leading edge injection requirement. With known free-stream pressure distribution and skin permeability, the strut was compartmented as shown in Figure 1 and pressures were selected for each compartment to best simulate the ideal injection distribution.

3. With skin permeability, compartment pressures, and free-stream static pressure distribution known, the actual injection distribution was calculated.

4. For the known injection distribution and free-stream aerodynamic conditions, the skin temperature analysis was performed using assumed values for the thermal conduction into the strut at each welded strut-skin interface.

5. The results of this analysis provided a first estimate of the temperatures at the interfaces, which were used to reestimate the conduction heat flow into the strut at each interface.

6. The strut thermal analysis was then performed using the calculated conduction heat flows as boundary conditions at each interface, assuming convection cooling of the strut itself.

7. The results of the strut analysis then provided a second estimate of the various strut-skin interface temperatures.

8. These interface temperature values were then individually compared to those obtained from the skin temperature analysis. Wherever disagreement was observed, the interface conduction heat flows were logically reestimated and the entire procedure was repeated starting with step 4.

9. Steps 4 through 8 were repeated until the interface temperatures obtained from the two independent analyses agreed within ± 1% at each attachment point. Since the heat flows were forced to match at each interface, agreement of temperatures would ensure a valid overall solution and energy balance.

DETERMINATION OF IDEAL INJECTION DISTRIBUTION

The ideal injection distribution which satisfied an isothermal skin temperature of 1700°F was calculated using the thermal analysis described in Appendix B. This analysis, based on the work of Reference 1, essentially matches the variation of the injection rate, $\rho_W v_W$, to that of the external heat transfer coefficient, h. This is apparent from Equation (B-3) of Appendix B, which shows that for $q_c = 0$, the ratio $h/\rho_W v_W$ must be constant to maintain a constant wall temperature, T_W. This implies that T_∞ and T_c are also constant.

In performing the analysis, subject to the assumptions presented in Appendix B, it was also assumed that the surface temperature was 1700°F at all locations including the strut weld regions. For purposes of determining the ideal injection distribution, the presence of the strut was ignored and heat flow into the strut was neglected.

The thermal effectiveness, η , which is a measure of the heat transfer efficiency of the porous wall itself was assumed to be 0.80 at all locations on the airfoil. The value of 0.80 was originally chosen simply because it was felt to be a reasonable value for a porous wall of this type. The usual assumption of $\eta = 1.0$ was felt to be optimistic and a certain conservatism in design is usually desirable. Since the design calculations for this study were made, limited data relative to the thermal effectiveness of Poroloy has become available (Reference 5). These data show considerable differences in the value of η for various Poroloy specimens. However, values of η both higher and lower than the assumed value of 0.80 were measured. Unfortunately, data for Poroloy of the particular permeability level specified in this design are lacking.

The boundary layer calculations as outlined in Appendix B were based on turbulent flow conditions for all regions of the airfoil except the leading edge. In the leading edge region, it was felt that a plane stagnation laminar flow exists, and the exact solutions which apply to this class of flow were employed (Reference 6). The results of these calculations are given in Figures 8a through 8c and will be discussed in a subsequent section of this report.

DETERMINATION OF COMPARTMENT DESIGN

The first step in determining a compartment design is to establish the permeability level of the porous skin. The Poroloy skin permeability level was to be chosen so as to satisfy the leading edge (stagnation point) injection requirement with an internal pressure of 44 psia. However, it was found that Bendix Filter Division is not presently fabricating or testing Poroloy which is permeable enough to satisfy this requirement. Therefore, the design was based on the most permeable Poroloy configuration currently being fabricated by Bendix. This configuration is characterized by the flow resistance curve corresponding to a permeability index value of 2×10^{-11} shown in Figure P. No. 039270 of Reference 2. The use of this wall permeability resulted in a required leading edge cavity internal pressure requirement of 52 psia as opposed to the specified or desired value of 44 psia.

The relationship between wall permeability, injection rate, and coolant pressure drop was based on the earlier work of Green (Reference 7) relative to sintered porous metals. Previous studies (Reference 4) have shown that fluid flow through Poroloy is governed by the same relationship originally developed by Green for sintered metals—e.g.,

$$\frac{\left(P_1^{\,2} - P_2^{\,2}\right) g}{\mu_c^{\,2} (2R\bar{T})} = \alpha' \frac{G_c}{\mu_c} + \beta' \left(\frac{G_c}{\mu_c}\right)^2 \qquad (1)$$

The resistance coefficients α' and β' depend on the permeability of a given porous structure and must be determined experimentally for each material of interest. In the present application, the coefficients α' and β' were determined from the experimental flow characteristics for Poroloy given in Reference 2. Using the values of α' and β' for the most permeable material currently being fabricated by Bendix, together with the required leading edge injection rate as calculated from Equation (B-3) of Appendix B and Reference 6, the supply pressure of 52 psia was calculated from Equation (1).

Having defined the wall permeability and coolant supply pressure in this manner, a basic compartment design could be established. The placement of the compartments and their respective internal pressures were chosen to best simulate the ideal injection distribution around the airfoil as shown in Figures 8a through 8c. The individual internal cavity pressures were calculated from Equation (1). The local values of G_c were obtained from Figures 8a through 8c and the local free-stream static pressures, P_2, from Figure 5. A certain degree of iteration was required in this process, and the compartment scheme shown in Figure 1 represents a reasonable compromise between mechanical complexity and effective thermal protection.

With the establishment of the various cavity pressures, together with the known local free-stream static pressures, the actual injection distribution was calculated using Equation (1). This distribution is shown in Figures 8a through 8c, where it is superimposed on the ideal distribution for comparison. The breaks in the actual distribution represent the strut locations where no physical blowing can occur. In general, the actual injection rates are larger than the ideal rates, indicating an overcooled situation. However, it must be noted that some overcooling of the regions adjacent to the strut is necessary to provide effective heat conduction away from the solid (zero injection) region of the weld.

The cavity pressures and injection rates previously established served to define the metering orifices in the base of each cavity. The calculated orifice sizes based on a supply (upstream of orifice) pressure of 52 psia and an assumed orifice coefficient of 0.70 are given in Table I, where the cavity designations correspond to those shown in Figure 1.

METHOD OF SKIN TEMPERATURE ANALYSIS

The skin temperature analysis in simplest terms involves the solution of Equation (B-3) of Appendix B, where the heat transfer coefficient, h, must reflect the various influences of injection, variable free-stream velocity, and variable surface temperature on thermal boundary layer development. The boundary layer calculations are outlined in Appendix B for the case of specified injection and free-stream velocity distributions.

The thermal conduction in the porous skin, q_c, is obtained by a two-dimensional finite difference calculation for an unfolded airfoil. To calculate the actual wall temperature distribution, it is assumed that in the trailing edge region of the airfoil the chordwise temperature distribution is symmetrical (i. e., no heat flows across the trailing edge from suction side to pressure side or vice versa). For analysis purposes, the airfoil can be envisioned as being cut along the trailing edge and unfolded so as to lay flat in the plane of the paper as shown in Figure 9.

The analysis is only two-dimensional with regard to conduction, but must include convection normal to these directions to account for gas-to-blade and blade-to-coolant heat transfer. The governing differential equation is the steady-state, two-dimensional heat conduction equation for systems without internal heat generation,

$$\frac{\partial}{\partial x}\left(k\frac{\partial T}{\partial x}\right)+\frac{\partial}{\partial y}\left(k\frac{\partial T}{\partial y}\right)=0 \tag{2}$$

where

T = temperature

k = temperature dependent thermal conductivity

x = chordwise direction

y = spanwise direction

For airfoil geometries and boundary conditions, it is not possible to obtain an exact solution to Equation (2) and a numerical technique must be used to obtain a solution. An exact solution of Equation (2) would yield an equation by which the temperature at any point of the airfoil could be calculated, while a numerical solution only yields temperatures at preselected, discrete points. The temperature at each of these points is considered to be representative of a certain region surrounding the point. It follows that one of the first steps in a numerical analysis of an airfoil is the subdivision of the airfoil into suitable regions. This is done by superimposing a grid of lines parallel to the x-y axes on a drawing of the unfolded airfoil. Each intersection of the lines provides a reference point which is referred to as a nodal point. The temperature at each nodal point is considered to be representative of the temperature of the surrounding material or node. The entire network of lines is often referred to as a mesh.

The equations to be solved numerically can be obtained by either writing the finite difference form of Equation (2) and its boundary conditions at each nodal point or by applying the conservation of energy principle to each node. The latter method is used herein. As an example, consider a five-node pattern such as that in Figure 10. The conservation of energy principle requires that in the steady-state the sum of the heat transferred into the center node must be equal to zero. For the node under consideration, the heat transferred into the node by conduction from the left is

$$k_1 A_1 \frac{(T_{i,\,j-1} - T_{i,\,j})}{\Delta x}$$

while the heat transferred into the node by conduction from the right is

$$k_2 A_2 \frac{(T_{i,\,j+1} - T_{i,\,j})}{\Delta x}$$

The heat transferred into the node by conduction from above is

$$k_3 A_3 \frac{(T_{i-1,\,j} - T_{i,\,j})}{\Delta y}$$

while heat transferred into the node by conduction from below is

$$k_4 A_4 \frac{(T_{i+1,\,j} - T_{i,\,j})}{\Delta y}$$

The heat transferred into the node by convection from the hot gas is

$$h_g \, \Delta x \, \Delta y \, (T_g - T_{i,\,j})$$

and the heat transferred from the coolant to the node is

$$\eta W_c \, C_{p_c} \, (T_c - T_{i,\,j})$$

where η accounts for cases where the wall effectiveness is less than 100% and W_c is the coolant flow rate through the i, j node. (See Appendix B.) It follows from the conservation of energy equation that

$$k_1 \; A_1 \frac{(T_{i,\,j-1} - T_{i,\,j})}{\Delta x} + k_2 \; A_2 \frac{(T_{i,\,j+1} - T_{i,\,j})}{\Delta x}$$

$$+ k_3 A_3 \frac{(T_{i-1, j} - T_{i, j})}{\Delta y} + k_4 A_4 \frac{(T_{i+1, j} - T_{i, j})}{\Delta y}$$

$$+ h_g \Delta x \Delta y (T_g - T_{i, j}) + \eta W_c Cp_c (T_c - T_{i, j}) = 0 \qquad (3)$$

This equation can be rearranged to give

$$- \frac{k_1 A_1}{\Delta x} T_{i, j-1} - \frac{k_3 A_3}{\Delta y} T_{i-1, j}$$

$$+ \left(\frac{k_1 A_1}{\Delta x} + \frac{k_2 A_2}{\Delta x} + \frac{k_3 A_3}{\Delta y} + \frac{k_4 A_4}{\Delta y} + h_g \Delta x \Delta y + \eta W_c Cp_c \right) T_{i, j}$$

$$- \frac{k_2 A_2}{\Delta x} T_{i, j+1} - \frac{k_4 A_4}{\Delta y} T_{i+1, j} = h_g \Delta x \Delta y T_g + \eta W_c Cp_c T_c \qquad (4)$$

For a porous material such as Poroloy, the question arises as to what values of k and A should be used. From a purely geometrical consideration, k should be the thermal conductivity of the base material and A should be the conduction area. Standard procedure for true porous materials is to relate the void to solid areas through a porosity P. If this procedure is followed, $A_1 = A_2 = (1-P_x) \Delta y \Delta z$ and $A_3 = A_4 = (1-P_y) \Delta x \Delta z$, where P_x is the ratio of void area to frontal area in the x-direction and P_y is the same for the y-direction. When these definitions are incorporated into Equation (4) along with the definition $W_c = G_c \Delta x \Delta y$, the result is

$$- k_1 (1-P_x) \frac{\Delta y \Delta z}{\Delta x} T_{i,j-1} - k_3 (1-P_y) \frac{\Delta x \Delta z}{\Delta y} T_{i-1, j}$$

$$+ \left[k_1 (1-P_x) \frac{\Delta y \Delta z}{\Delta x} + k_2 (1-P_x) \frac{\Delta y \Delta z}{\Delta x} + k_3 (1-P_y) \frac{\Delta x \Delta z}{\Delta y} \right.$$

$$\left. + k_4 (1-P_y) \frac{\Delta x \Delta z}{\Delta y} + h_g \Delta x \Delta y + \eta G_c Cp_c \Delta x \Delta y \right] T_{i, j}$$

$$- k_2 (1-P_x) \frac{\Delta y \Delta z}{\Delta x} T_{i, j+1} - k_4 (1-P_y) \frac{\Delta x \Delta z}{\Delta y} T_{i+1, j}$$

$$= h_g \Delta x \Delta y T_g + \eta G_c Cp_c \Delta x \Delta y T_c \qquad (5)$$

When equations such as Equation (5) are written for every node of the mesh, a set of n equations in the n unknown nodal point temperatures is obtained. The resulting set of simultaneous equations can then be solved using conventional over-relaxation numerical techniques as discussed in References 8 and 9. In performing the skin temperature analysis, constant porosity values (P_x, P_y) of 0.68 were assumed throughout. The base metal thermal conductivities (k_1, k_2, k_3, k_4) were assumed to vary with temperature as follows:

Skin temperature (°F)	Thermal conductivity (BTU/hr-ft-°F)
1200	12.6
1400	13.8
1600	15.1
1800	16.2

The two-dimensional heat conduction calculation previously outlined can be related to the boundary layer calculation outlined in Appendix B by noting that the first four terms of Equation (3) correspond to the term q_c in Equation (B-3). The boundary conditions applied to this problem include zero heat flux across the trailing edge surfaces and assumed constant temperature at the root and tip sections. The constant temperature condition is in lieu of heat flow conditions at these surfaces which would require an additional thermal analysis of the end attachments. Experience has indicated that the constant temperature condition can be assigned with sufficient accuracy to provide good overall prediction of skin metal temperatures.

At those locations where the strut is welded to the skin, the wall is solid and no actual injection occurs. However, since some heat flows into the strut by conduction, it was necessary to account for this heat flow in the weld regions. If reference is made to Equation (3), it will be noted that the last term represents a heat sink. It was possible, therefore, to simulate the conduction heat flow into the strut by assigning a ficticious injection rate, G_c, to those segments (nodes) of the wall where it is welded to the strut. When the solution of Equation (3) was obtained, the heat sink term then provided a direct measure of the conduction heat flow into the strut, which in turn was used as a boundary condition for the independent thermal analysis of the strut. The strut analysis is discussed in the following section.

METHOD OF STRUT TEMPERATURE ANALYSIS

The thermal analysis of the strut was treated in a manner similar to that of the skin in that a two-dimensional finite difference heat conduction analysis was applied to the problem. However, in the case of the strut, the plane of heat flow is defined by a cross section of the strut itself. To facilitate the analysis, the cross section of the strut (mean line) was approximated by the rectangular nodal network shown in Figure 11.

The basic approach to the analysis was the finite difference solution of Equation (1) subject to specified boundary conditions on all of the external boundaries. Heat flux boundary conditions were applied to each boundary shown as a dotted line in Figure 11, which was used to approximate the welded strut-skin interface. The numerical values of the heat flows at each interface (dotted line) were estimated from the fictitious conduction heat flows calculated in the skin temperature analysis previously outlined. The remaining solid line portions of the strut boundary represent the interior surfaces of the compartments (coolant channels). Convective boundary conditions for the strut-to-coolant heat transfer were applied to these surfaces. Convective heat transfer coefficients for each channel were based on an equivalent hydraulic diameter of the channel section at the mean line. Using the previously established coolant flow rate for each channel, numerical values of the heat transfer coefficients were obtained using a conventional correlation (Reference 10), which assumes fully developed turbulent flow.

The two-dimensional thermal analysis of the strut was performed at the meanline (midspan) section only. Consequently, several assumptions were employed.

1. The coolant total pressure and flow rate at the meanline section are the same as at the base or coolant entrance plane.

2. Temperature rise of the coolant caused by heat pickup from the strut was neglected. Thus, a coolant (heat sink) temperature of 1200°F was used for all convective boundary conditions.

3. Although the strut analysis was performed only at the mean section, it was assumed that the conduction heat flow from the skin to the strut was the same at all spanwise locations and equal to the value at the mean section.

The latter assumption implies that the temperature pattern calculated for the strut mean section would also apply at the hub and tip.

Subject to the boundary conditions and assumptions listed previously, the two-dimensional temperature pattern in the strut was determined from a solution of the n simultaneous heat balance equations written for the n nodal points of the simulated strut. Again, successive over-relaxation techniques were employed (References 8 and 9). In particular, the temperatures at the dotted boundaries (Figure 11) representing the strut skin interface were determined and compared to the temperatures at the same location calculated in the skin temperature analysis previously outlined. Since the heat flow at each interface was forced to match that calculated in the skin temperature analysis, agreement of temperatures at each interface would represent a valid solution of the coupled skin-strut problem.

At all locations where these temperatures did not agree, the skin temperature analysis was repeated using adjusted values for the simulated conduction heat flow. The strut analysis was also repeated using new conduction heat flux boundary conditions as calculated from the repeated skin temperature analysis. Again, local interface temperatures were compared and the overall procedure was repeated until satisfactory agreement was obtained at all skin-strut interfaces. As previously mentioned, this procedure was applied at the mean section only. To calculate skin temperatures at other spanwise locations, the conduction heat flow rates to the strut were assumed the same (as those for the mean section) at all spanwise locations. The following tabulated strut thermal conductivities were used in all calculations.

Temperature (°F)	Thermal conductivity (BTU/hr-ft-°F)
1400	14.90
1600	18.25
1800	27.80
2000	30.00

Numerical results relative to strut and skin temperature patterns are presented in the following section.

NUMERICAL RESULTS AND DISCUSSION

Ideal Injection Distribution and Compartmentation Design

The calculated injection distributions required to maintain an isothermal 1700°F skin temperature are shown in Figures 8a through 8c. The leading edge injection rate reflects the large stagnation point heat fluxes which usually occur in a turbine vane. The rapid variation in injection rate near the leading edge reflects the rapid variation of free-stream velocity as well as the assumed early transition from laminar to turbulent flow. The spanwise variation in the injection rates primarily reflect the gas temperature profile (Figure 7).

The final compartment design, chosen to provide simulation of the ideal injection distribution, is shown in Figures 1 through 3. The various compartment pressures and inlet orifice areas are given in Table I, where the cavity designations correspond to those shown in Figure 1. Generally, the required cavity pressures in the trailing edge compartments are lower than those in the forward portion of the airfoil reflecting the lower free-stream static pressures in the trailing edge region.

The actual injection distributions, calculated as outlined under Determination of Compartment Design, are shown superimposed on Figures 8a through 8c for comparison with the ideal distribution. As previously noted, the actual injection rates are generally larger than the ideal rates, indicating an overcooling of most porous wall regions. This is desirable to a degree, however, in providing effective (chordwise) conduction cooling of the solid weld regions. The sawtooth profile of the actual injection distribution results from the interruption of blowing by the weld segments, and also reflects the fact that the wall permeability and/or cavity pressure cannot be continuously varied to match the changing free-stream static pressures.

Integration of the injection rates over the vane chord and span results in a predicted actual coolant flow of 5.3% based on a gas flow of 0.805 lb_m/sec per vane channel.

Calculated Temperature Distributions—Design Condition

The coupled, iterative solution for skin and strut temperatures, as previously outlined, resulted in satisfactory convergence of the strut and skin temperatures at all welded interfaces. The final solution for the skin temperatures is shown in Table II, which is a computer printout of the two-dimensional temperature distribution of the unwrapped airfoil. The rows and columns shown in Table II correspond to the nodal network of the unwrapped airfoil shown in Figure 12. The rows which correspond to the regions of the strut-skin weld are identified by arrows. They are rows 4, 10, 15, 19, 24, 30, 34, 38, 43, and 47. The skin temperature results are also represented in terms of an isotherm plot in Figure 13. This isotherm plot was prepared by an Orthomat Digital Plotting Machine which used the temperature pattern of Table II as input. It is not as accurate as the printout, Table II, but is useful in defining trends, hotspots, etc.

A survey of the skin temperature results indicates that all skin temperatures, including strut weld locations, are less than 1740°F. The maximum overall temperature difference on a given side is about 350°F. Although the maximum temperature of 1740°F is slightly above the desired maximum temperature of 1700°F, the design is considered to be acceptable, especially since the mean skin temperature is well below 1700°F. The maximum gradient of 350°F is somewhat larger than would be desired. However, limited experience with porous wall airfoils in the past indicates that such gradients are acceptable and should not seriously compromise blade life. It should be noted that the constant temperature of 1700°F at the hub and tip sections was assigned as the boundary condition previously noted. Since the solution indicates that these temperatures are generally higher than those of adjacent rows, the assigned temperature of 1700°F was apparently too high. In the subsequent analysis at the off-design condition, these assigned boundary temperatures were revised downward to 1600°F as will be shown later. As previously mentioned, the somewhat artificial manipulation of the hub and tip boundary temperatures does not seriously affect the calculated metal temperatures because the influence is felt only in the adjacent rows. Since the temperatures in the adjacent rows are quite low because of the gas temperature profile, the assigned boundary conditions do not alter the conclusion regarding acceptability of the overall vane design.

The final strut temperature distribution at the design condition is tabulated in Table III, where the key to each location is given on the vane-strut cross section shown in Figure 1. An isotherm pattern for the strut cross section is given in Figure 14 for defining the temperature distribution trends. As noted previously, these results are for the mean section only, but should not differ by more than about ±40°F from those at the hub and tip section. This difference is based on the observed spanwise skin temperature variation at the attachment regions (Table II). In Table III, the skin temperatures at the strut-skin interface are shown in parentheses. These skin temperatures correspond to those in row 6 (mean line) of Table II for the columns representing strut locations. Table III gives the locations of the strut-skin interfaces and indicates that the strut and skin temperatures are in close agreement, indicating a valid solution of the coupled problem. The maximum overall strut temperature is approximately 1720°F, while the minimum value is about 1520°F. These temperatures are acceptable from a design standpoint as indicated in the Stress Analysis section.

Calculated Injection Distributions — Off-Design Condition

As previously discussed, the off-design condition differs from the design condition only in the increase of the gas-stream total pressure from 42 to 105 psia. Because of the change in gas-stream pressure level, it was necessary to increase the cooling air supply pressure to ensure positive flow to all coolant compartments. It was found that a coolant supply pressure of 115 psia would be adequate for the present design.

Since the orifice area in the base of each cavity was fixed to satisfy the design condition, it was necessary to establish each individual cavity pressure at a level which would simultaneously satisfy the orifice flow as well as the total flow through the porous wall segment defined by that cavity. Because the two flows must be equal, only one cavity pressure would satisfy this requirement subject to the specified supply pressure and local external free-stream static pressures. The cavity pressures were thus established by a simultaneous solution of the standard orifice flow equation and the porous wall flow relationship for each cavity—Equation (1). Since the external static pressures, P_2, varied spanwise and chordwise for a given segment, it was necessary to break each porous wall segment into a number of small regions, applying Equation (1) simultaneously to each region. It was assumed again that the internal pressure was constant throughout the entire cavity.

The off-design cavity pressures and flows calculated in this manner are shown in Table IV, where the cavity designations correspond to those shown in Figure 1. The total vane coolant flow rate was 4.9% based on a gas-stream flow of 2.013 lb_m/sec per vane.

The off-design injection distribution was calculated as outlined previously for the design condition, using the cavity pressures shown in Table IV. In these calculations, the local free-stream static pressures were obtained from Figure 5, where all local pressure values were increased by a factor of 2.5 (105/42). The injection results are shown in Figures 15a through 15c. The pattern is similar to that for the design condition (Figures 8a through 8c) except that the general level is increased, reflecting the increased off-design pressure level.

Calculated Temperature Distributions—Off-Design Condition

The skin and strut temperatures for the off-design condition were calculated in the same manner as for the design condition. The printout of skin temperatures is given in Table V, with the corresponding isotherm plot shown in Figure 16. The strut temperature distribution for the mean section is shown in Table VI.

Inspection of the results shows that, in general, local temperatures at the strut-skin interfaces are higher than those at the design condition by about 100°F. Similarly, the average strut temperature is about 100°F higher at the off-design condition. These differences are caused by the large increases in gas-to-wall heat fluxes associated with the increases in gas-stream total pressure level. Along those portions of the wall which are actively cooled, the increased local injection rates essentially compensate for the higher heat fluxes—i.e., coolant and mainstream density levels increase in an almost one-to-one ratio. However, for those sections of the wall which are welded, the increased coolant heat transfer rates along the strut channels do not directly compensate for the large gas-to-wall heat fluxes because of the larger thermal resistance of the strut conduction cooling mechanism. As a direct consequence, heat flow into the weld regions is impeded, resulting in increased local surface temperatures in these areas.

At the off-design condition, skin temperatures vary from a maximum of 1922°F to a minimum of 1326°F. Local strut temperatures range from 1872°F to 1530°F for the same conditions. These temperatures considerably exceed the desired design metal temperature limit of 1700°F. Consequently, extended operation of the vane at the off-design condition is not recommended. At a maximum temperature over 1900°F, the Poroloy skin would probably oxidize quite rapidly based on limited experimental data (Reference 4). Strut life would also be reduced because of the increased maximum temperature and thermal gradient. In general, extended operation at the off-design condition would require lower cooling air temperatures and/or higher flow rates to reduce maximum temperatures to the levels encountered at the design condition.

STRESS ANALYSIS

SKIN DEFLECTION CALCULATION

Because of the pressure difference across those sections of the Poroloy skin between strut support points, some estimate of skin deflection and bending stress was deemed advisable. Therefore, the maximum positive bending stress and deflection for the Poroloy skin was calculated based on a simplified theory for restrained beams. To use this approach, it was assumed that the porous skin between two supporting struts could be approximated by a beam fixed at both ends and carrying a uniformly distributed load.

For the proposed design (Figure 1), the maximum unsupported surface length between two struts is about 0.6 in. and the wall thickness is 0.025 in. Since the span is approximately 4 in., the moment of inertia about the neutral axis is 5.2×10^{-6} in.^{4} The largest pressure drop across the wall at any point (design condition) is approximately 10 psi. Since the pressure drop across any skin segment is essentially constant in the chordwise direction, a uniform beam loading of 40 lb/in. (based on a 4-in. span) was used. The modulus of elasticity for the Poroloy skin was assumed to be 4.5×10^6 psi.

Based on these parameters, the maximum deflection was found to be 0.0006 in. and the maximum positive bending stress was 1450 psi. These values are considered to be acceptable and no additional calculations were made.

VANE STRUT STRESS ANALYSIS

The maximum bending stress was also calculated for the Poroloy vane strut. Gas pressure loads of 7.22 and 39.24 lb parallel to and normal to the airfoil tangent line, respectively, were obtained from an integration of the static pressure distributions (Figure 5) over the airfoil surfaces. Based on the strut design presented on NASA drawing CR650677, end attachments were determined to be fixed at one end, and free but guided at the other end. The applicable moment equation, therefore, is

$$\begin{aligned}\text{Maximum moment} &= \omega s^2/3 \\ &= 39.24 \times 4.5/3 \\ &= 58.9 \text{ in.-lb}\end{aligned}$$

The maximum stress was calculated to be

$$\begin{aligned}\text{Maximum stress} &= Mc/I \\ &= 58.9 \times 0.3/0.00234 \\ &= 7545 \text{ psi}\end{aligned}$$

The maximum bending stress of 7545 psi can be compared to the stress rupture limit of cast U-700 at 1700°F, which is approximately 22,000 psi based on a 400-hr life. The anticipated bending stress, therefore, is well within the allowable limit and the strut design is considered to be acceptable for the specified design conditions. The actual boundary condition at the free end is probably some combination of the free but guided condition and the free but simply supported condition. Since in the latter case the maximum bending moment is $1/8\,\omega s^2$, the results given by Equations (6) and (7) can be considered conservative.

APPENDIX A

LIST OF SYMBOLS

A	laminar boundary layer similarity parameter
A_n (n = 1, 4)	nodal conduction heat flow areas for finite difference calculation
A_1	turbulent boundary layer similarity parameter
B	laminar boundary layer similarity parameter
B_1	turbulent boundary layer similarity parameter
C_p	specific heat
c	strut moment arm (neutral axis)
Eu	Euler No.
F_1	laminar flow Stanton No. coefficient
F_2	turbulent flow Stanton No. coefficient
f_w	injection parameter
G_c	coolant flow rate per unit face area (injection rate)
g	gravitational constant
f_w'	turbulent boundary layer blowing parameter
h, h_g	heat transfer coefficient between hot gas and wall
I	moment of inertia of strut
k	thermal conductivity
k_n (n = 1, 4)	directional thermal conductivities for finite difference calculation
k_w	thermal conductivity of air evaluated at the porous wall surface temperature

ℓ	characteristic length of surface over which boundary layer is calculated
M	maximum bending moment on strut caused by the gas pressure load
Nu_x	Nusselt No., hx/k_w
n	surface temperature gradient parameter
Pr	Prandtl No.
P_1	coolant pressure on upstream side of porous wall (coolant pressure inside airfoil)
P_2	local static pressure downstream of porous wall (local free-stream static pressure)
$P_3{}'$, $P_5{}'$	turbulent boundary layer integral relations
P_n $(n = 1, 5)$	laminar boundary layer integral relations defined in Equations (B-16) and (B-17)
P_x, P_y	directional porous wall porosity factors relating to effective conduction heat flow area
q_c	net heat flow by conduction
q_r	heat flow by radiation
R	gas constant
Re_x	Reynolds No., $(\rho_w U_\infty x)/\mu_w$
Re_ℓ	Reynolds No. based on ℓ
Re_ϕ	Reynolds No. based on ϕ
S	airfoil span length
St	local Stanton No., $h/(\rho_\infty U_\infty Cp_\infty)$
St_o	turbulent flow Stanton No. for flat plate flow with zero injection
T	temperature
$\bar{T}$	mean coolant temperature inside porous wall

T_c	coolant supply temperature
T_{cw}	coolant temperature at exit from porous wall
T_g, T_∞	gas-stream temperature
$T_{i,\ j}$	local wall temperature
T_w	porous wall surface temperature
$\bar{T}_w$	$T_w - T_\infty$
U_o	upstream (undisturbed) free-stream velocity
U_∞	local free-stream velocity
u	component of boundary velocity in x direction
v	component of boundary layer velocity in y direction
v_w	component of boundary layer velocity in y direction at interface between porous wall and external boundary layer ($y = 0$)
W_c	coolant flow rate
x	axial or chordwise distance from leading edge
y	spanwise distance
	the distance of any location in the boundary layer from the wall (Appendix B)
z	distance measured through blade wall
α	exponent of specific heat—temperature variation, $Cp \sim T^{\alpha}$
α'	porous wall flow resistance coefficient
β	exponent of viscosity—temperature variation, $\mu \sim T^{\beta}$
β'	porous wall flow resistance coefficient
Δx, Δy	chordwise and spanwise dimensions of each nodal point on unwrapped airfoil for finite difference conduction analysis

η	effectiveness of porous wall
θ_1	dimensionless wall temperature, $(T_\infty - T_w)/(T_w - T_c)$
θ_w	dimensionless wall temperature, $(T_\infty - T_w)/(T_\infty - T_c)$
μ	fluid viscosity
ξ	dimensionless distance, x/ℓ
ρ	fluid density
ϕ	convection thickness for boundary layer, $\int_0^\infty \left[\left(\frac{\rho u}{\rho_\infty U_\infty}\right)\left(\frac{T - T_\infty}{T_w - T_\infty}\right)\right] dy$
ω	average airfoil gas pressure load per unit span length

Subscripts

c	coolant supply conditions
g, ∞	gas-or free-stream conditions
w	conditions at surface of porous wall

APPENDIX B

HEAT TRANSFER ANALYSIS FOR TRANSPIRATION COOLED WALLS

BASIC APPROACH

The problem of calculating heat transfer in transpiration cooled boundary layers with arbitrary injection, pressure gradient, and surface temperature distributions is treated in this Appendix. The basic physical model and control volume for energy conservation is shown schematically in Figure 17. The analytical model is based primarily on the integral form of the boundary layer thermal energy equation. However, the essential feature of the model is the development of a logical relationship between the local Stanton No. and boundary layer thermal convection thickness. This relationship permits calculation of a local convection thickness which reflects the cumulative effects of pressure gradient, surface temperature, and injection distribution on boundary layer development. In this respect, the approach is unified—i.e., applicable to both laminar and turbulent flows.

This Appendix is based on the work of Reference 1, and is subject to the following restrictions or assumptions.

1. Radiation effects are negligible.
2. Consideration is restricted to flows where viscous dissipation is negligible.
3. In laminar flow, fluid properties are assumed to have a simple power law temperature dependence. However, turbulent flow results are restricted to constant fluid properties.
4. The analysis is restricted to air or to fluids having properties nearly the same as air.
5. The laminar flow analysis is restricted to a wall Prandtl No. of 0.70.
6. The variation in coolant specific heat caused by fluid temperature rise across the porous wall is neglected.

The basic approach to the general problem is to calculate the growth of the thermal boundary layer along the surface in question. The local values of the Stanton No. or heat transfer coefficient can be related to the thermal boundary layer growth and permit calculation of the heat flux from the boundary layer to the wall. The heat flux to the wall must be absorbed by the coolant flowing through the wall and is related, therefore, to the coolant flow rate and the temperature rise of the coolant (Figure 17). Mathematically, the problem involves the simultaneous solution of three equations.

1. The integral form of the boundary layer thermal energy conservation equation which provides a means of calculating the thermal boundary layer development.

2. An expression relating the thermal boundary layer development to the local Stanton No.

3. An energy balance equation which relates the wall heat flux to the coolant heat absorption.

These three equations are sufficient to calculate any of the quantities of interest—e.g., given an arbitrarily specified injection rate distribution, the local heat flux and surface temperature are determined. Conversely, if the surface temperature distribution and free-stream velocity distribution are arbitrarily specified, the local heat flux and injection rate are uniquely determined. The analysis of this problem requires simultaneous consideration of the heat transfer processes both within the wall and within the external boundary layer. The two regions are highly coupled because both the injection rate (and distribution) and surface temperature distribution affect boundary layer development, which in turn influences the local heat transfer rate and surface temperature.

The boundary layer problem is treated by considering the mean or integrated form of the boundary layer differential equation representing thermal energy conservation. This equation is integrated across the boundary layer to obtain an overall rather than a local conservation of energy within the boundary layer. If viscous dissipation effects are neglected, the integral equation becomes (Reference 1)

$$\frac{d\phi}{dx} + \phi \left[\frac{1}{U_\infty} \frac{dU_\infty}{dx} + \frac{1}{\overline{T}_W} \frac{d\overline{T}_W}{dx} \right] - \frac{Cp_W}{Cp_\infty} \frac{\rho_W v_W}{\rho_\infty U_\infty} = St\,(x) \qquad \text{(B-1)}$$

In deriving Equation (B-1), the integral $(\int Cp \rho u (T - T_\infty)\,dy$ is divided through by $\rho_\infty U_\infty Cp_\infty (T_W - T_\infty)$, where U_∞ and T_W can vary with x in an arbitrary manner. To obtain the convection thickness, ϕ, it is assumed that this integral may be approximated by $\overline{Cp} \int \rho\, u(T - T_\infty)\,dy$ and further, that the ratio $\overline{Cp}_\infty \approx 1.0$. Since the specific heat varies with temperature, Cp is not a constant across the boundary layer and Equation (B-1) is only an approximation. However, Cp is a weak function of temperature and this approximation results in little error. Equation (B-1) represents a first-order, linear, ordinary differential equation for the convection thickness, $\phi(x)$. For specified values of $U_\infty(x)$, $\overline{T}_W(x)$, and $v_W(x)$ and a knowledge of how St varies with x, Equation (B-1) can be integrated to determine $\phi(x)$. In general, however, the Stanton No. depends locally on $\bar{T}_W$, v_W, U_∞, and x; also $\bar{T}_W$ and v_W cannot be independently specified.

Because the variation of the Stanton No. with x is different depending on the previous history of the boundary layer—i.e., on the upstream effects of $T_W(x)$, $v_W(x)$, and $U_\infty(x)$—the local variation of St will be expressed as a function of ϕ. Thus,

$$St = St(x) = g\left[\phi(x)\right] \tag{B-2}$$

where $\phi(x)$ depends on n, x, f_W, Eu, and T_W. When St is represented as in Equation (B-2), Equation (B-1) and an overall heat balance equation are sufficient to solve the general problem. For specified $v_W(x)$ and $U_\infty(x)$, $T_W(x)$ and $\phi(x)$ are determined by simultaneous solution of these two equations. Conversely, for specified $T_W(x)$ and $U_\infty(x)$, $\phi(x)$ and $v_W(x)$ are determined.

An energy balance for the porous wall element shown in Figure 17 may be written as

$$h\left[T_\infty - T_W\right] = \rho_W v_W Cp_W \left[T_{cW} - T_c\right] \pm q_c \pm q_r \tag{B-3}$$

If radiative heat transfer effects are neglected and it is assumed that the fluid temperature rise is some fraction η of the maximum possible rise, then Equation (B-3) becomes

$$h\left[T_\infty - T_W\right] = \rho_W v_W Cp_W \left[T_W - T_c\right] \eta \pm q_c \tag{B-4}$$

where

$$\frac{T_{cW} - T_c}{T_W - T_c} = \eta$$

Equations (B-1) through (B-4) are the basic working equations of the analysis and their solution is discussed in the following paragraphs for the cases of interest.

LAMINAR FLOWS

An important step in developing this approach is to determine the function $g\left[\phi(x)\right]$ in Equation (B-2). It is assumed that the relationship between the Stanton No. and convection thickness may be obtained from the exact similarity solutions. Since each is a unique function of n, Eu, f_W, T_W/T_∞, Pr_W, and x, elimination of x provides a relationship between St and ϕ which depends on the local values of n, Eu, f_W, T_W/T_∞, and Pr_W. The crucial assumption here is that the relationship between St and ϕ (derived for constant values of the parameters n, Eu, f_W, T_W/T_∞, and Pr_W) is valid locally even when these parameters vary with x in a smooth but arbitrary manner.

The relationships for $\phi(x)$ and St(x) obtained from the similarity solutions are given in References 6, 11, and 12. They are rewritten here for convenience as

$$\phi/x\sqrt{Re_x} = A\ (f_w,\ Eu,\ n,\ T_w/T_\infty,\ Pr_w) \tag{B-5}$$

and

$$Nu_x/\sqrt{Re_x} = B\ (f_w,\ Eu,\ n,\ T_w/T_\infty,\ Pr_w) \tag{B-6}$$

where the functions A and B are known from the exact solutions as developed in References 6, 11, and 12. By eliminating x from Equations (B-5) and (B-6) and defining the Stanton No. as

$$St = \frac{h}{\rho_\infty U_\infty Cp_\infty} \tag{B-7}$$

the following equation can be obtained:

$$St = AB\,(Re_\phi)^{-1}\ (Pr_w)^{-1}\ \frac{\rho_w\ Cp_w}{\rho_\infty\ Cp_\infty} \tag{B-8}$$

where $Re_\phi = \rho_w\ U_\infty \phi/\mu_w$.

At this point, it is convenient to introduce an assumed power law property variation* so that (B-8) becomes

$$St = AB\,(Re_\phi)^{-1}\ (Pr_w)^{-1}\ (T_w/T_\infty)^{a-1} \tag{B-9}$$

A reference Reynolds No. is also introduced as

$$Re_\ell = \frac{\rho_\infty U_o \ell}{\mu_\infty} \tag{B-10}$$

where U_o is some upstream (undisturbed) velocity and ℓ is a characteristic dimension of the particular system of interest. Using Equation (B-10), Equation (B-9) becomes

$$St = F_1 \left[Re_\ell \left(\frac{\phi}{\ell}\right)\left(\frac{U_\infty}{U_o}\right)\right]^{-1} (Pr_w)^{-1}\left(\frac{T_w}{T_\infty}\right)^{a+\beta} \tag{B-11}$$

---

*It is assumed that $\rho \sim T^{-1}$, $Cp \sim T^{a}$, and $\mu \sim T^{\beta}$.

where

$$F_1 = AB$$

Employing Equation (B-11), Equation (B-1) becomes

$$\frac{d\phi}{dx} + \phi\left[\left(\frac{1}{U_\infty}\right)\left(\frac{dU_\infty}{dx}\right) + \left(\frac{1}{\bar{T}_w}\right)\left(\frac{d\bar{T}_w}{dx}\right)\right] - \frac{Cp_w\,\rho_w\,v_w}{Cp_\infty\,\rho_\infty\,U_\infty} = \frac{F_1\left(\dfrac{T_w}{T_\infty}\right)^{\alpha+\beta}}{Re_\ell\left(\dfrac{\phi}{\ell}\right)\left(\dfrac{U_\infty}{U_o}\right)Pr_w} \tag{B-12}$$

Tabulated values for the function F_1 may be found in Table VII.

The various similarity parameters f_w, Eu, and n are defined as

$$f_w \equiv \frac{\rho_w\,v_w}{\rho_\infty\,U_\infty}\left[Re_\ell\left(\frac{U_\infty}{U_o}\right)\left(\frac{x}{\ell}\right)\right]^{0.5}\left(\frac{2}{Eu+1}\right)\left(\frac{T_w}{T_\infty}\right)^{(1-\beta)/2} \tag{B-13}$$

$$Eu \equiv \frac{x}{U_\infty}\;\frac{dU_\infty}{dx} \tag{B-14}$$

$$n \equiv \left(\frac{x}{T_\infty - T_w}\right)\left[\frac{d(T_\infty - T_w)}{dx}\right] \tag{B-15}$$

The solution of Equations (B-1) through (B-4), or alternately Equations (B-11), (B-12), and (B-4), is discussed in the following paragraphs for the two cases of interest.

θ_w (x) and U_∞ (x) Specified

When $\theta_w(x)$ and $U_\infty(x)$ are specified, Equations (B-11), (B-12), and (B-4) may be used to evaluate St(x) and $\rho_w\,v_w(x)$. The first step in the solution is to indicate formally the integration of Equation (B-12). First, the term $\dfrac{Cp_w\,\rho_w\,v_w}{Cp_\infty\,\rho_\infty U_\infty}$ in Equation (B-12) is eliminated using Equation (B-4). Then, using an integrating factor, Equation (B-12) may be integrated to yield

$$\frac{\phi}{\ell} = \left\{ \left(\frac{U_\infty}{U_o} \theta_w \right)^{-2} \left[\left(\frac{\phi}{\ell} \right)_o^2 \left(\frac{U_\infty}{U_o} \theta_w \right)_o^2 + P_5 (\xi) \right] \right\}^{1/2} \tag{B-16}$$

where

$$P_4 (\xi) = \left[\frac{2 \left(\frac{U_\infty}{U_o} \theta_w \right)^2}{Re_\ell \; Pr_w} \right] \left[\frac{F_1 \left(\frac{T_w}{T_\infty} \right)^{\alpha + \beta}}{\frac{U_\infty}{U_o}} \right] \left(\frac{\theta_1}{\eta} + 1 \right)$$

$$P_5 (\xi) = \int_o^\xi P_4 (\xi) \, d\xi$$

$$\xi = \frac{x}{\ell}$$

Equation (B-16) cannot be evaluated until $P_5 (\xi)$ is known and $P_5 (\xi)$ depends on F_1, which in turn depends on f_w and hence on $\rho_w v_w (x)$. To obtain a solution, an initial estimate of the distribution $f_w(x)$ is made. Since Eu, T_w/T_∞, and Pr_w are known or specified, F_1 can be evaluated and $P_5(\xi)$ can be determined. Knowing $P_5 (\xi)$, $\phi/\ell (\xi)$ can be found from Equation (B-16) and used in Equation (B-11) to evaluate St (ξ). Equation (B-4) is then used to calculate $\rho_w v_w$ (x) which can be used in Equation (B-13) to reestimate $f_w(\xi)$. The procedure is then repeated until $f_w (\xi)$ converges satisfactorily. In the computer analysis, the actual surface of interest is broken up into n intervals and the iteration previously outlined is carried out at each station i. When $f_w (\xi_i)$ has converged, $f_w(\xi_{i+1})$ is estimated and the iteration is carried out until $f_w(\xi_{i+1})$ converges; then $f_w(\xi_{i+2})$ is estimated and continued up to ξ_n. The relationship for F_1 is handled in the computer analysis as a multi-dimension table lookup with appropriate interpolation.

$\rho_w v_w$ (x) and U_∞ (x) Specified

When $\rho_w v_w(x)$ and U_∞ (x) are specified, Equations (B-11), (B-12) and (B-4) are solved to yield St(x) and $\theta_w(x)$. The solution proceeds in a similar manner to that previously outlined with some exceptions. Integrating (B-12) now yields

$$\frac{\phi}{\ell} = \left\{ \left(\frac{U_\infty}{U_o} \theta_w \right)^{-2} \left[\left(\frac{\phi}{\ell} \right)_o^2 \left(\frac{U_\infty}{U_o} \theta_w \right)_o^2 + P_3 (\xi) \right] \right\}^{1/2} \tag{B-17}$$

where

$$P_3(\xi) = \int_o^{\xi} \left[P_1(\xi) + P_2(\xi)\right] d\xi$$

$$P_1(\xi) = \frac{2\left(\frac{U_\infty}{U_o}\ \theta_w\right)^2}{Re_\ell\ Pr_w}\left[\frac{F_1\left(\frac{T_w}{T_\infty}\right)^{\alpha+\beta}}{\left(\frac{U_\infty}{U_o}\right)}\right]$$

$$P_2(\xi) = 2\left(\frac{U_\infty}{U_o}\ \theta_w\right)^2\left(\frac{\phi}{\ell}\right)\left(\frac{\rho_w v_w}{\rho_\infty U_\infty}\right)\left(\frac{T_w}{T_\infty}\right)^{\alpha}$$

Again, Equation (B-17) cannot be immediately evaluated because θ_w, ϕ/ℓ, and T_w/T_∞ are not known. To obtain a solution, $\theta_w(\xi)$ and $\phi/\ell(\xi)$ are initially estimated; $\phi/\ell(\xi)$ must be estimated first to evaluate $P_2(\xi)$. Using the estimated value of $\theta_w(\xi)$, $T_w/T_\infty(\xi)$ can be found and together with $\rho_w v_w(\xi)$ permits the evaluation of $f_w(\xi)$ from Equation (B-13) and hence, F_1. Then, $P_3(\xi)$ can be evaluated and $\phi/\ell(\xi)$ determined from Equation (B-17). The calculated value of $\phi/\ell(\xi)$ can be used in Equation (B-11) and (B-4) to reestimate $\theta_w(\xi)$. The calculated values of $\theta_w(\xi)$ and $\phi/\ell(\xi)$ are used to reestimate $P_3(\xi)$ and the procedure is repeated to convergence.

TURBULENT FLOWS

For the case of a turbulent boundary layer, Equations (B-1)through (B-4) still apply, but the relationship indicated in Equation (B-2) is different from laminar flow. In the case of turbulent flow, this relationship becomes

$$St = F_2\left[Re_\ell\left(\frac{\phi}{\ell}\right)\left(\frac{U_\infty}{U_o}\right)\right]^{-1/4}(Pr_\infty)^{-2/3} \qquad \text{(B-18)}$$

The parameter F_2 is derived in a similar manner to F_1 and is given by

$$F_2 = B_1\,(A_1)^{1/4} \qquad \text{(B-19)}$$

where

$$B_1 = \frac{Nu_x}{(Re_x)^{4/5}}\,(Pr_\infty)^{-1/3} \qquad \text{(B-20)}$$

$$A_1 = (\phi/x)\,(Re_x)^{1/5} \qquad \text{(B-21)}$$

The parameters A_1 and B_1 are functions of the same parameters that influence the corresponding laminar flow solution, namely $f_w{}'$, Eu, T_w/T_∞, n, and Pr. Numerical values for B_1 are derived from Rubesin's analysis (Reference 13), while A_1 is derived from the solution of Equation (B-1) using Equation (B-20) to evaluate the Stanton No. (See Reference 1.) Tabulated values of the parameter F_2 are given in Table VIII. The turbulent flow injection parameter is given by

$$f_w{}' = \frac{\rho_w v_w}{\rho_\infty U_\infty} (St_o)^{-1} \tag{B-22}$$

where to good approximation

$$St_o = 0.0288 \left(\frac{\rho_\infty U_\infty x}{\mu_\infty}\right)^{-1/5} (Pr_\infty)^{-2/3} \tag{B-23}$$

The solution of Equations (B-1), (B-4), and (B-18) is handled exactly as for laminar flow. For the case where $\rho_w v_w(x)$ is specified, integration of Equation (B-1), using Equation (B-18), yields

$$\frac{\phi}{\ell} = \left\{\left(\frac{U_\infty}{U_o}\theta_w\right)^{-5/4} \left[\left(\frac{\phi}{\ell}\right)_o^{5/4} \left(\frac{U_\infty}{U_o}\theta_w\right)_o^{5/4} + P_3{}'(\xi)\right]\right\}^{4/5} \tag{B-24}$$

where

$$P_3{}'(\xi) = \int_o^{\xi} \left\{\frac{5}{4}\left(\frac{U_\infty}{U_o}\theta_w\right)^{5/4} \left(\frac{\phi}{\ell}\right)^{1/4} \left(\frac{\rho_w v_w Cp_w}{\rho_\infty U_\infty Cp_\infty}\right) + \frac{5}{4}\left(\frac{F_2 (Pr_\infty)^{-2/3}}{(Re_\ell)^{1/4}\left(\frac{U_\infty}{U_o}\right)^{1/4}}\right)\left(\frac{U_\infty}{U_o}\theta_w\right)^{5/4}\right\} d\xi$$

Again, initial estimates of $\theta_w(\xi)$ and $\phi/\ell(\xi)$ are made and the iteration is carried out as previously outlined.

For the case where $\theta_w(x)$ is specified, integrating Equation (B-1) yields

$$\frac{\phi}{\ell} = \left\{\left(\frac{U_\infty}{U_o}\theta_w\right)^{-5/4} \left[\left(\frac{\phi}{\ell}\right)_o^{5/4} \left(\frac{U_\infty}{U_o}\theta_w\right)_o^{5/4} + P_5{}'(\xi)\right]\right\}^{4/5} \tag{B-25}$$

where

$$P_5'(\xi) = \int_0^{\xi} \left[\frac{5}{4} \left(\frac{U_\infty}{U_o} \theta_w \right)^{5/4} \left(\frac{F_2 \; (Pr_\infty)^{-2/3}}{(Re_\ell)^{1/4} \left(\dfrac{U_\infty}{U_o} \right)^{1/4}} \right) \left(\frac{\theta_1}{\eta} + 1 \right) \right] d\xi$$

Again, the required iteration on f_w' is carried out as previously outlined.

REFERENCES

1. Nealy, D. A. An Approximate Treatment of Heat Transfer in Plane Laminar and Turbulent Flows Over Arbitrary Surfaces With Arbitrary Surface Injection—Including Wall Conduction Effects, Ph. D. thesis, Purdue University, June 1968.

2. Wheeler, Jr., H. L. Transpiration Cooling in the High Temperature Gas Turbine. Bendix Corporation. March 1964.

3. Huppert, M. C. and MacGregor, C. Comparison Between Predicted and Observed Performance of Gas Turbine Stator Blade Design for Free-Vortex Flow. NACA TN 1810, 1949.

4. Anderson, R. D. and Nealy, D. A. Evaluation of Laminated Porous Material for High-Temperature Air-Cooled Turbine Blades—Final Report Tasks I and II (U). NASA CR 72281, January 1967 (Confidential).

5. Nealy, D. A. and Anderson, R. D. Heat Transfer Characteristics of Laminated Porous Materials (U). Air Force Systems Command. AFAPL TR-68-98. August 1968 (Confidential).

6. Brown, W. B. and Donoughe, P. L. Tables of Exact Laminar Boundary Layer Solutions When the Wall is Porous and Fluid Properties are Variable. NACA TN 2479, 1951.

7. Green, Jr., L. and Duwez, P. "Fluid Flow Through Porous Metal." Journal of Applied Mechanics (ASME). Vol 18, No. 1 (1951), pp. 39-45.

8. Varga, R. S. Matrix Iterative Analysis. Englewood Cliffs, New Jersey: Prentice-Hall, Inc, 1962.

9. Curre, B. A. "The Determination of the Optimum Accelerating Factor for Successive Over-Relaxation." Journal of Computing. Vol 4, No. 1, 1961.

10. Kreith, F. Principles of Heat Transfer. 1st ed. Scranton, Pa: International Textbook Co, 1958, pp. 346-349.

11. Brown, W. B. "Exact Solutions of the Laminar Boundary Layer Equations for a Porous Plate with Variable Fluid Properties and a Pressure Gradient in the Mainstream." Proceedings, First U. S. National Congress of Applied Mechanics, 1951.

12. Livingood, J. N. B. and Donoughe, P. L. Summary of Laminar Boundary Layer Solutions for Wedge-Type Flow Over Convection and Transpiration Cooled Surfaces. NACA TN 3588, 1955.

13. Rubesin, M. W. An Analytical Estimation of the Effect of Transpiration Cooling on the Heat Transfer and Skin Friction Characteristics of a Compressible Turbulent Boundary Layer. NACA TN 3341, 1954.

Table I.

Design condition cavity pressures and orifice areas.

Cavity	Pressure (psia)*	Orifice area (in.^{2})
A	49.0	0.0339
B	40.0	0.0125
C	36.0	0.00905
D	34.0	0.0153
E	34.0	0.00763
F	35.0	0.0110
G	38.0	0.007
H	40.0	0.00873
I	43.0	0.00865
J	43.0	0.00865

---

* Supply pressure—52 psia

Table II.

Tabulated values of skin temperatures for the design condition.

	1	2	3	↓ 4	5	6	7	8
1	1700.00	1700.00	1700.00	1700.00	1700.00	1700.00	1700.00	1700.00
2	1535.52	1539.64	1571.61	1714.70	1610.69	1580.84	1570.80	1569.42
3	1506.95	1512.29	1548.15	1705.37	1585.28	1552.14	1541.91	1541.99
4	1485.29	1490.93	1529.09	1697.47	1563.38	1528.27	1518.97	1520.56
5	1464.36	1470.48	1510.87	1690.26	1544.38	1507.65	1498.73	1500.80
6	1445.79	1452.35	1494.67	1683.78	1526.60	1488.28	1479.80	1483.41
7	1423.81	1431.17	1475.64	1674.51	1505.38	1465.92	1458.42	1463.66
8	1404.91	1412.86	1459.08	1666.74	1486.65	1446.18	1439.53	1446.11
9	1389.03	1397.39	1444.86	1659.98	1470.22	1428.91	1422.94	1430.59
10	1383.97	1392.27	1439.36	1658.19	1462.23	1421.26	1415.99	1424.13
11	1700.00	1700.00	1700.00	1700.00 ↑	1700.00	1700.00	1700.00	1700.00

Note: Row and column numbers correspond to nodal network shown in Figure 12.
Arrows denote those columns where strut ribs are welded to airfoil skin.

Table II. (Cont)

9	↓ 10	11	12	13	14		↓ 15	16
1700.00	1700.00	1700.00	1700.00	1700.00	1700.00	1	1700.00	1700.00
1587.05	1680.98	1573.56	1543.61	1527.56	1551.19	2	1625.20	1557.14
1564.00	1673.01	1553.33	1521.72	1507.69	1530.95	3	1618.21	1542.39
1546.01	1667.76	1538.07	1505.67	1493.81	1516.52	4	1615.42	1532.34
1526.06	1645.65	1519.61	1489.29	1480.19	1503.43	5	1612.68	1522.96
1514.19	1657.60	1508.73	1474.57	1466.92	1490.71	6	1610.70	1514.74
1497.70	1652.33	1495.56	1461.22	1454.98	1481.81	7	1609.27	1512.88
1482.72	1646.60	1483.15	1448.83	1443.92	1473.68	8	1607.68	1511.25
1469.42	1641.97	1471.95	1437.54	1433.83	1466.23	9	1606.46	1509.92
1463.69	1641.85	1467.69	1434.00	1431.38	1465.36	10	1609.68	1513.55
1700.00	1700.00 ↑	1700.00	1700.00	1700.00	1700.00	11	1700.00 ↑	1700.00

Table II. (Cont)

17	18	↓ 19	20	21	22	23	↓ 24
1700.00	1700.00	1700.00	1700.00	1700.00	1700.00	1700.00	1700.00
1570.25	1604.08	1661.49	1507.81	1496.86	1521.73	1580.41	1740.50
1558.17	1594.50	1657.45	1505.38	1498.21	1528.08	1588.32	1732.68
1549.35	1589.32	1657.01	1507.84	1504.75	1539.97	1599.55	1724.75
1540.85	1583.79	1658.02	1512.29	1513.93	1554.11	1612.45	1716.51
1533.06	1578.90	1658.28	1515.70	1522.28	1568.06	1628.10	1709.88
1534.06	1583.00	1657.73	1522.73	1531.83	1578.03	1636.95	1707.52
1535.46	1587.68	1656.25	1529.66	1542.33	1589.06	1646.60	1705.34
1537.23	1593.03	1656.12	1537.58	1553.21	1600.90	1656.81	1701.71
1543.45	1601.80	1658.45	1549.47	1567.94	1616.00	1669.55	1701.28
1700.00	1700.00	1700.00 ↑	1700.00	1700.00	1700.00	1700.00	1700.00 ↑

Table II. (Cont,

25	26	27	28		29	↓ 30	31	32
1700.00	1700.00	1700.00	1700.00	1	1700.00	1700.00	1700.00	1700.00
1441.03	1425.47	1490.20	1427.45	2	1439.44	1644.48	1601.73	1570.87
1437.03	1416.68	1483.73	1418.38	3	1434.41	1649.63	1595.81	1562.88
1436.73	1413.10	1482.04	1413.14	4	1425.19	1605.93	1580.44	1556.70
1436.18	1409.60	1481.02	1411.10	5	1434.35	1667.93	1595.77	1561.47
1435.67	1406.13	1479.76	1407.49	6	1434.31	1676.25	1596.35	1560.97
1436.21	1410.10	1480.46	1407.53	7	1434.79	1679.45	1595.51	1559.04
1436.82	1414.11	1481.20	1407.52	8	1434.67	1679.27	1593.75	1556.76
1437.26	1418.12	1482.03	1407.64	9	1434.64	1679.14	1592.00	1553.81
1442.62	1427.56	1488.11	1413.78	10	1439.69	1681.98	1595.63	1557.37
1700.00	1700.00	1700.00	1700.00	11	1700.00	1700.00 ↑	1700.00	1700.00

Table II. (Cont)

33	↓ 34	35	36	37	↓ 38	39	40	41
1700.00	1700.00	1700.00	1700.00	1700.00	1700.00	1700.00	1700.00	1700.00
1556.36	1577.83	1507.71	1481.59	1486.25	1578.54	1608.58	1585.43	1558.33
1550.95	1584.96	1502.51	1473.33	1478.03	1574.31	1594.74	1569.81	1543.11
1550.26	1597.86	1503.95	1471.98	1476.15	1574.81	1585.13	1558.66	1532.60
1554.30	1613.99	1507.63	1472.43	1475.80	1578.26	1578.21	1550.01	1523.93
1556.45	1629.50	1510.61	1472.23	1474.81	1579.40	1570.48	1540.73	1514.80
1555.23	1634.66	1508.60	1467.83	1470.64	1581.36	1557.91	1525.37	1499.67
1553.41	1638.01	1505.81	1463.34	1466.50	1582.69	1546.52	1510.81	1485.74
1547.89	1625.97	1499.69	1458.41	1462.76	1585.17	1536.18	1498.00	1473.50
1555.42	1650.69	1507.28	1462.06	1466.32	1593.35	1532.71	1493.08	1468.89
1700.00	1700.00	1700.00	1700.00	1700.00	1700.00	1700.00	1700.00	1700.00
	↑				↑			

Table II. (Cont)

```
                   ↓                                         ↓
    42            43       44       45       46       47       48       49       50

1700.00  1 1700.00  1700.00  1700.00  1700.00  1700.00  1700.00  1700.00  1700.00

1558.15  2 1668.20  1598.48  1562.60  1570.22  1724.77  1644.58  1581.19  1542.07

1544.54  3 1661.67  1579.25  1540.16  1549.09  1714.13  1612.20  1547.15  1509.91

1535.44  4 1658.36  1564.52  1522.45  1532.59  1704.36  1584.71  1518.74  1484.85

1527.87  5 1655.89  1551.47  1507.36  1518.21  1697.46  1561.68  1494.65  1462.94

1520.54  6 1653.77  1538.65  1493.28  1504.15  1690.48  1539.77  1473.09  1442.75

1507.77  7 1650.95  1521.55  1474.96  1487.73  1683.60  1517.94  1450.11  1421.37

1495.59  8 1647.55  1506.18  1457.76  1472.97  1677.60  1498.82  1429.93  1402.79

1484.54  9 1646.17  1492.39  1442.68  1459.95  1672.16  1480.84  1412.28  1386.88

1480.80 10 1648.82  1485.50  1436.30  1454.86  1671.62  1471.72  1405.12  1381.77

1700.00 11 1700.00  1700.00  1700.00  1700.00  1700.00  1700.00  1700.00  1700.00
              ↑                                         ↑
       CALC TIME (MINUTES)     11.172
```

Table III.

Strut temperature pattern at the mean section for the design condition.

Location	Temperature (°F)
1	1713 (1710)
2	1653 (1658)
3	1614 (1611)
4	1660 (1658)
5	1698 (1684)
6	1700
7	1713 (1690)
8	1660 (1654)
9	1570 (1579)
10	1635 (1630)
11	1686 (1676)
12	1634
13	1620
14	1637
15	1560
16	1522
17	1548
18	1546
19	1558
20	1620
21	1603
22	1617
23	1678

Table IV.

Off-design cavity pressures and flow rates.

Cavity designation	Orifice area (in.^{2})	Pressure (psia)*	Flow rate (lb_m/sec)
A	0.0339	109.2	0.0160
B	0.0125	93.5	0.0105
C	0.00905	83.8	0.00856
D	0.0153	77.1	0.0152
E	0.00763	77.1	0.0076
F	0.0110	82.0	0.0151
G	0.007	87.7	0.00631
H	0.00873	94.0	0.00723
I	0.00865	101.7	0.00594
J	0.00865	101.7	0.00594

---

*Supply pressure—115.0 psia

Table V.

Tabulated values of skin temperatures for the off-design condition.

	1	2	3	↓ 4	5	6	7	8
1	1600.00	1600.00	1600.00	1600.00	1600.00	1600.00	1600.00	1600.00
2	1474.50	1474.94	1516.98	1850.10	1665.67	1619.48	1598.46	1586.13
3	1439.17	1441.03	1486.95	1842.46	1617.03	1569.27	1551.45	1542.01
4	1412.50	1415.29	1462.65	1832.02	1573.30	1524.72	1510.16	1505.23
5	1391.45	1394.88	1443.08	1823.77	1537.93	1489.11	1476.75	1473.60
6	1374.78	1378.66	1427.31	1817.72	1506.66	1457.16	1446.58	1445.53
7	1357.69	1362.29	1411.22	1810.00	1475.30	1426.58	1418.73	1420.38
8	1345.56	1350.52	1399.17	1803.81	1450.27	1402.26	1396.37	1399.90
9	1337.45	1342.51	1390.44	1798.81	1430.39	1383.06	1378.55	1383.34
10	1335.37	1340.24	1386.32	1792.61	1416.58	1370.80	1367.31	1372.74
11	1600.00	1600.00	1600.00	1600.00	1600.00	1600.00	1600.00	1600.00
				↑				

Note: Row and column numbers correspond to nodal network shown in Figure 12.

Arrows denote those columns where strut ribs are welded to airfoil skin.

Table V. (Cont)

9	↓ 10	11	12	13	14	↓ 15	16
1600.00	1600.00	1600.00	1600.00	1600.00	1600.00	1600.00	1600.00
1601.24	1795.31	1567.26	1522.16	1498.35	1545.02	1717.08	1505.87
1563.92	1789.94	1538.23	1493.32	1473.21	1515.25	1715.16	1489.36
1532.60	1783.17	1511.90	1467.01	1451.02	1490.85	1712.70	1474.20
1504.34	1777.24	1488.11	1444.39	1432.18	1468.18	1710.41	1461.19
1480.11	1772.38	1468.13	1425.17	1416.19	1449.39	1709.44	1449.81
1458.34	1766.81	1451.39	1409.92	1403.14	1439.19	1708.86	1447.96
1440.30	1762.72	1437.14	1396.84	1391.86	1430.19	1708.68	1446.44
1425.32	1759.03	1424.93	1385.65	1382.13	1422.13	1708.25	1445.05
1414.92	1754.74	1416.43	1378.63	1376.31	1416.91	1707.77	1445.37
1600.00	1600.00	1600.00	1600.00	1600.00	1600.00	1600.00	1600.00
	↑					↑	

Table V. (Cont)

17	18	↓ 19	20	21	22	23	↓ 24
1600.00	1600.00	1600.00	1600.00	1600.00	1600.00	1600.00	1600.00
1519.48	1581.00	1773.22	1437.76	1420.56	1448.30	1524.09	1875.14
1505.67	1570.34	1773.88	1439.34	1427.54	1463.77	1543.75	1871.41
1492.69	1560.85	1767.96	1442.21	1437.58	1482.83	1568.67	1864.69
1481.56	1552.85	1776.61	1448.44	1450.63	1505.43	1597.53	1858.03
1470.80	1544.16	1777.96	1453.30	1464.48	1531.07	1632.84	1854.09
1473.71	1554.77	1776.20	1463.34	1479.59	1550.99	1654.11	1852.23
1477.10	1566.48	1779.12	1475.15	1495.98	1572.41	1678.67	1850.83
1480.71	1578.48	1779.83	1488.06	1513.80	1595.93	1706.66	1847.00
1485.82	1590.82	1779.40	1503.75	1535.38	1623.50	1739.62	1844.09
1600.00	1600.00	1600.00 ↑	1600.00	1600.00	1600.00	1600.00	1600.00 ↑

Table V. (Cont)

25	26	27	28	29	↓ 30	31	32
1600.00	1600.00	1600.00	1600.00	1600.00	1600.00	1600.00	1600.00
1416.72	1463.75	1563.32	1469.48	1442.56	1808.47	1921.97	1882.32
1420.46	1463.24	1562.66	1468.70	1443.78	1810.61	1856.81	1800.81
1425.94	1464.32	1562.93	1469.40	1446.42	1811.36	1801.73	1732.53
1432.26	1465.65	1563.27	1470.30	1449.80	1815.92	1759.27	1684.81
1439.93	1467.28	1563.69	1471.40	1453.69	1822.01	1724.18	1649.35
1441.31	1467.76	1563.80	1471.64	1453.81	1820.95	1709.30	1633.05
1442.80	1468.32	1563.92	1471.85	1453.74	1818.49	1695.96	1618.80
1444.12	1468.93	1564.07	1472.09	1453.73	1816.38	1684.32	1606.01
1447.00	1470.97	1565.08	1473.77	1454.91	1812.94	1673.93	1594.59
1600.00	1600.00	1600.00	1600.00	1600.00	1600.00	1600.00	1600.00
					↑		

Table V. (Cont)

33	↓ 34	35	36	37	↓ 38	39	40	41
1600.00	1600.00	1600.00	1600.00	1600.00	1600.00	1600.00	1600.00	1600.00
1790.43	1713.43	1571.27	1500.00	1480.00	1652.22	1811.96	1704.91	1602.40
1723.33	1715.74	1552.46	1484.46	1468.17	1646.49	1763.84	1662.87	1573.31
1673.64	1720.26	1536.49	1472.03	1459.01	1640.97	1719.32	1625.63	1547.29
1639.15	1728.16	1524.25	1461.47	1451.27	1637.21	1678.68	1594.15	1524.00
1613.84	1737.47	1514.84	1452.07	1445.69	1643.24	1647.40	1567.84	1503.96
1600.60	1739.51	1503.46	1439.33	1433.75	1634.31	1602.63	1530.24	1474.20
1588.51	1741.78	1493.15	1428.39	1424.54	1634.62	1568.40	1498.23	1448.14
1577.87	1746.84	1483.80	1418.93	1416.84	1636.48	1541.28	1473.10	1426.87
1567.61	1745.12	1476.44	1412.94	1412.33	1638.95	1518.47	1453.35	1411.75
1600.00	1600.00 ↑	1600.00	1600.00	1600.00	1600.00 ↑	1600.00	1600.00	1600.00

Table V. (Cont)

	↓				↓			
42	43	44	45	46	47	48	49	50
1600.00	1600.00	1600.00	1600.00	1600.00	1600.00	1600.00	1600.00	1600.00
1570.93	1817.75	1735.77	1634.99	1605.74	1875.09	1693.04	1566.84	1490.55
1548.43	1807.65	1680.82	1586.59	1564.91	1860.07	1625.54	1510.27	1447.14
1528.86	1796.82	1635.14	1544.47	1517.52	1818.24	1559.61	1465.15	1413.83
1511.31	1789.22	1598.98	1511.79	1502.01	1832.35	1529.98	1431.53	1388.93
1495.02	1782.33	1568.78	1483.94	1478.04	1823.73	1496.48	1404.10	1369.61
1470.60	1775.27	1528.89	1449.00	1451.75	1815.82	1464.22	1379.71	1351.77
1450.63	1770.54	1497.67	1421.27	1430.97	1809.19	1439.15	1361.31	1338.82
1434.39	1767.13	1470.60	1399.27	1414.64	1804.22	1419.58	1347.62	1329.77
1422.89	1763.27	1450.42	1384.46	1403.63	1798.19	1406.24	1340.47	1326.71
1600.00	1600.00	1600.00	1600.00	1600.00	1600.00	1600.00	1600.00	1600.00
	↑				↑			

Table VI.

Strut temperature pattern at the mean section for the off-design condition.

Location	Temperature (°F)
1	1872 (1854)
2	1762 (1778)
3	1705 (1709)
4	1772 (1772)
5	1820 (1818)
6	1819
7	1840 (1824)
8	1775 (1782)
9	1635 (1643)
10	1742 (1737)
11	1835 (1822)
12	1768
13	1708
14	1732
15	1590
16	1530
17	1600
18	1587
19	1604
20	1700
21	1684
22	1740
23	1810

Table VII.

Tabulation of F_1 function.*

(Part A: $n = 0$ and $Pr_w = 0.70$)

f_w	$T_w/T_\infty = 0.25$			$T_w/T_\infty = 0.50$			$T_w/T_\infty = 1.0$		
	Eu = 0	Eu = 0.5	Eu = 1.0	Eu = 0	Eu = 0.5	Eu = 1.0	Eu = 0	Eu = 0.5	Eu = 1.0
0	0.786	0.909	0.939	0.441	0.540	0.575	0.244	0.330	0.352
0.10	0.728	0.853	0.873	0.411	0.520	0.541	0.228	0.316	0.334
0.25	0.639	0.770	0.775	0.364	0.477	0.492	0.204	0.294	0.310
0.40	0.549	0.685	0.673	0.317	0.433	0.442	0.179	0.273	0.286
0.50	0.488	0.625	0.610	0.285	0.403	0.407	0.162	0.258	0.269
0.60	0.420	0.567	0.540	0.250	0.373	0.373	0.143	0.243	0.252
0.70	0.351	0.516	0.471	0.214	0.341	0.338	0.124	0.227	0.234
0.80	0.277	0.442	0.402	0.176	0.308	0.303	0.105	0.211	0.216
0.90	0.196	0.375	0.328	0.135	0.274	0.266	0.083	0.194	0.196
1.00	0.105	0.306	0.253	0.088	0.239	0.226	0.059	0.177	0.176

(Part B: $T_w/T_\infty = 1.0$ and $Pr_w = 0.70$)

f_w	$n = 0$			$n = 0.50$			$n = 1.0$		
	Eu = 0	Eu = 0.5	Eu = 1.0	Eu = 0	Eu = 0.5	Eu = 1.0	Eu = 0	Eu = 0.5	Eu = 1.0
0	0.244	0.329	0.350	0.234	0.336	0.360	0.220	0.330	0.358
0.50	0.162	0.258	0.269	0.162	0.282	0.300	0.152	0.282	0.306
1.00	0.0593	0.177	0.176	0.0675	0.224	0.232	0.0641	0.232	0.248

* Tabulated values are based on the results of Reference 6.

Table VIII.

Tabulation of F_2 function. *

($n = 0$ and $T_w/T_\infty = 1.0$)

f_w'	Eu = -0.5	Eu = 0	Eu = 0.5	Eu = 1.0
0.00	0.0158	0.0133	0.0120	0.0112
0.20	0.0152	0.0128	0.0115	0.0107
0.40	0.0142	0.0122	0.0110	0.0102
0.60	0.0136	0.0114	0.0103	0.0096
0.80	0.0127	0.0107	0.0096	0.0090
1.00	0.0118	0.0099	0.0090	0.0084
1.20	0.0110	0.0093	0.0084	0.0078
1.40	0.0102	0.0086	0.0077	0.0072
1.60	0.0092	0.0078	0.0070	0.0065
1.80	0.0085	0.0071	0.0064	0.0060
2.00	0.0079	0.0066	0.0060	0.0056
2.20	0.0073	0.0062	0.0056	0.0052
2.40	0.0067	0.0057	0.0051	0.0048
2.60	0.0062	0.0052	0.0047	0.0044
2.80	0.0057	0.0048	0.0043	0.0040
3.00	0.0052	0.0044	0.0040	0.0037

*Tabulated values are based on the results of Reference 13.

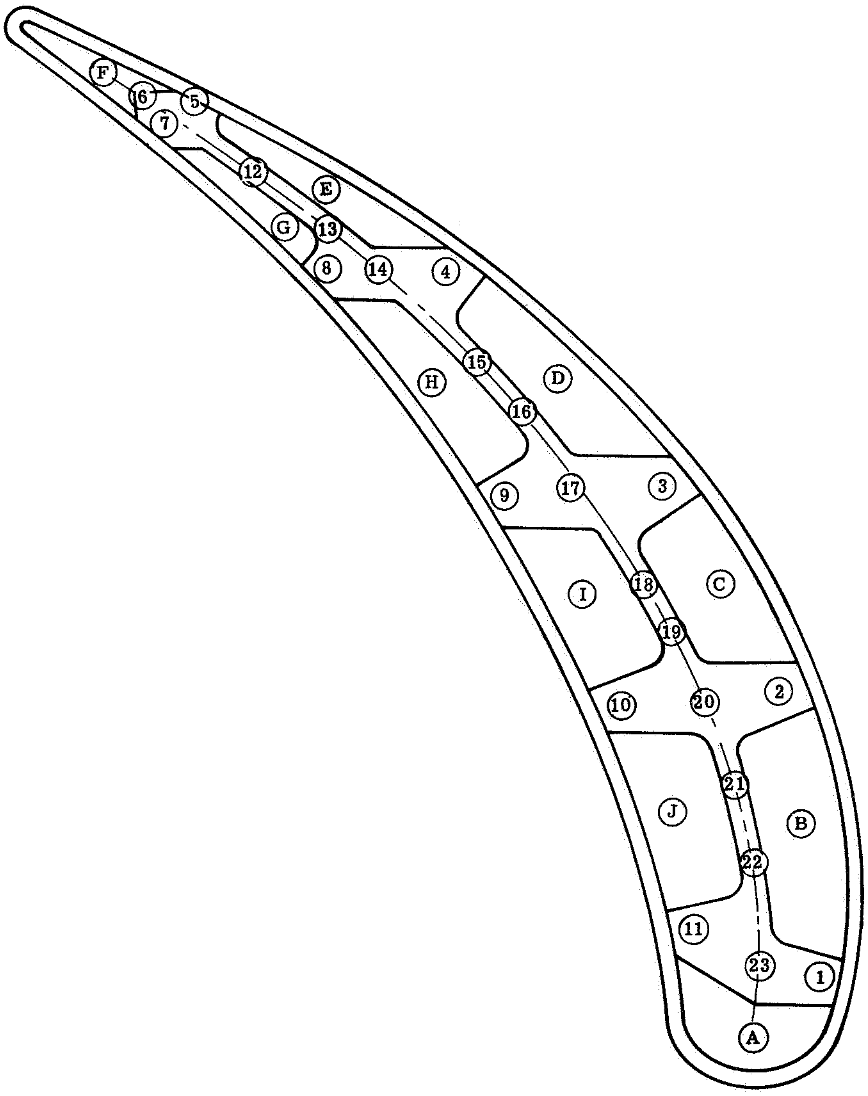

5923-1

Figure 1. Poroloy vane and strut mean section.

SECTION	B-B		C-C		D-D	
Point Z X	1.0390		1.0280		1.0120	
Point Z Y	0.2610		0.3330		0.4040	
θ	28°46'		33°33'		38°20'	
R_1	0.1600		0.1600		0.1600	
R_2	0.0350		0.0340		0.0330	
X	Y_L	Y_U	Y_L	Y_U	Y_L	Y_U
0.0000	0.1600	0.1600	0.1600	0.1600	0.1600	0.1600
0.1000	—	0.3190	—	0.3230	—	0.3370
0.2000	0.0050	0.3900	0.0060	0.4080	0.0060	0.4290
0.3000	0.0430	0.4500	0.0500	0.4730	0.0570	0.4950
0.4000	0.0770	0.4970	0.0930	0.5230	0.1080	0.5430
0.5000	0.1050	0.5360	0.1270	0.5600	0.1480	0.5760
0.6000	0.1320	0.5660	0.1560	0.5870	0.1770	0.6010
0.7000	0.1560	0.5870	0.1800	0.6060	0.1990	0.6190
0.8000	0.1770	0.6010	0.1970	0.6190	0.2140	0.6300
0.9000	0.1940	0.6100	0.2110	0.6240	0.2270	0.6330
1.0000	0.2070	0.6110	0.2220	0.6240	0.2350	0.6310
1.1000	0.2160	0.6060	0.2310	0.6190	0.2400	0.6240
1.2000	0.2210	0.5950	0.2350	0.6080	0.2430	0.6120
1.3000	0.2240	0.5800	0.2360	0.5900	0.2420	0.5940
1.4000	0.2230	0.5600	0.2330	0.5690	0.2380	0.5710
1.5000	0.2200	0.5340	0.2270	0.5410	0.2280	0.5420
1.6000	0.2120	0.5030	0.2170	0.5080	0.2170	0.5070
1.7000	0.2010	0.4670	0.2050	0.4720	0.2020	0.4700
1.8000	0.1860	0.4260	0.1890	0.4310	0.1830	0.4270
1.9000	0.1670	0.3820	0.1690	0.3840	0.1610	0.3800
2.0000	0.1440	0.3340	0.1440	0.3340	0.1370	0.3280
2.1000	0.1180	0.2830	0.1150	0.2800	0.1100	0.2740
2.0000	0.0870	0.2290	0.0830	0.2230	0.0810	0.2150
2.3000	0.0550	0.1710	0.0480	0.1620	0.0460	0.1550
2.4000	0.0200	0.1120	0.0120	0.0980	0.0090	0.0910
2.4600	—	—	—	—	0.0330	0.0330
2.4700	—	—	0.0340	0.0340	—	—
2.4930	0.0350	0.0350	—	—	—	—

Note: All dimensions are in inches.

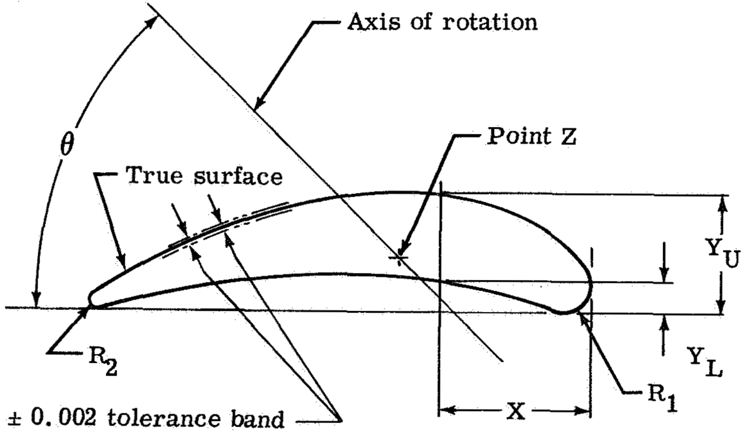

Figure 2. Airfoil coordinates.

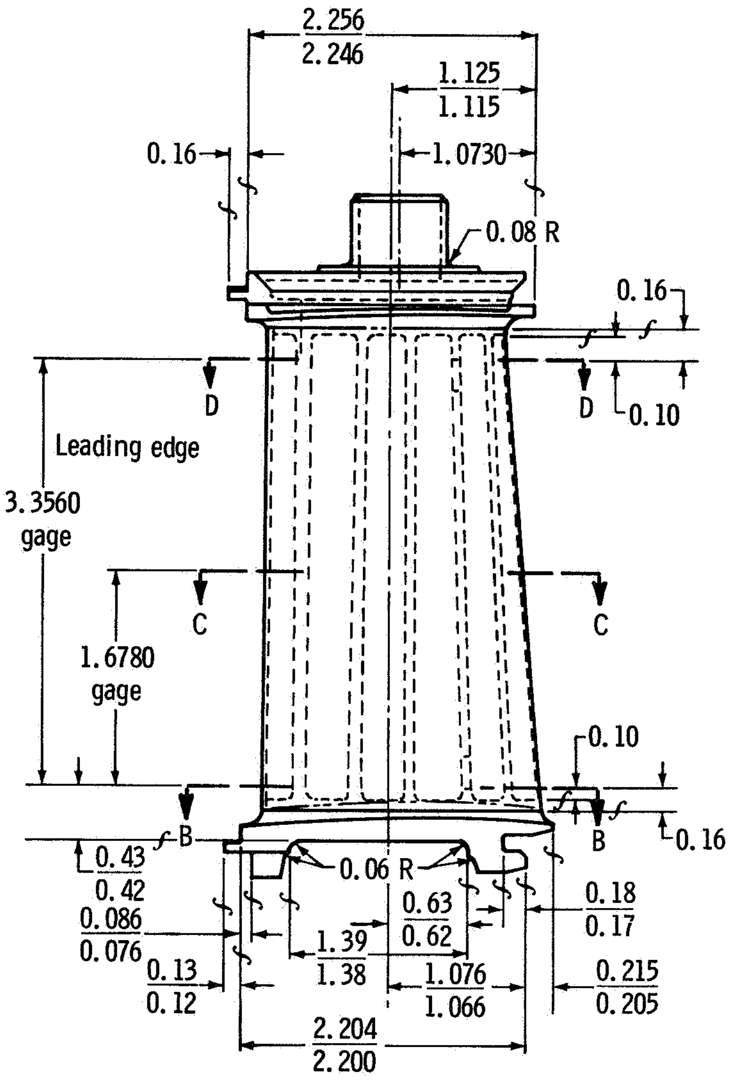

Note: All dimensions are in inches.

STRUT COORDINATES

STATION NO.	SECTION B-B A*	SECTION B-B B*	SECTION D-D A	SECTION D-D B
1	0.2730	0.3790	0.2330	0.3920
2	0.3070	0.3180	0.2760	0.3400
3	0.3710	0.2960	0.3480	0.3210
4	0.5800	0.3650	0.5370	0.3960
5	0.6150	0.4140	0.5720	0.4430
6	0.5950	0.5120	0.5510	0.5370
7	0.6880	0.5320	0.6500	0.5600
8	0.7410	0.4420	0.1200	0.4700
9	0.8100	0.4120	0.7950	0.4450
10	0.9800	0.4280	0.9280	0.4560
11	1.0290	0.4680	0.9770	0.4980
12	1.0350	0.5530	0.9850	0.5840
13	1.1400	0.5500	1.0940	0.5730
14	1.1900	0.4580	1.1690	0.4770
15	1.2560	0.4260	1.2520	0.4420
16	1.5200	0.3940	1.4560	0.4140
17	1.5750	0.4240	1.5160	0.4400
18	1.5840	0.4590	1.5290	0.4760
19	1.6900	0.4240	1.6580	0.4310
20	1.7160	0.3740	1.6980	0.3780
21	1.7900	0.3280	1.8000	0.3200
22	2.0350	0.2440	2.0000	0.2480
23	2.1030	0.2380	2.0600	0.2460
24	0.3960	0.1280	0.3840	0.1600
25	0.3730	0.1990	0.3480	0.2240
26	0.3990	0.2590	0.3700	0.2800
27	0.6100	0.3280	0.5760	0.3590
28	0.6720	0.3070	0.6460	0.3410
29	0.7210	0.2160	0.7150	0.2560
30	0.8160	0.2320	0.8070	0.2720
31	0.8030	0.3190	0.7960	0.3580
32	0.8360	0.3700	0.8370	0.4020
33	1.0440	0.3880	0.9820	0.4120
34	1.1140	0.3560	1.0600	0.3800
35	1.1600	0.2720	1.1260	0.2940
36	1.2580	0.2760	1.2340	0.2940
37	1.2520	0.3400	1.2280	0.3560
38	1.2930	0.3800	1.2700	0.3990
39	1.5950	0.3340	1.5200	0.3550
40	1.6670	0.2930	1.6160	0.3030
41	1.6910	0.2520	1.6480	0.2600
42	1.7900	0.2380	1.7560	0.2400
43	1.7950	0.2520	1.7580	0.2530
44	1.8430	0.2720	1.8070	0.2730
45	2.0130	0.2100	1.9500	0.2230
46	2.0830	0.1740	2.0360	0.1790
47	2.0910	0.1560	2.0500	0.1620
48	0.1760	0.3000	0.1480	0.3020
49	0.2880	0.0980	0.2800	0.1420
50	2.1910	0.1950	2.1500	0.1970
51	2.1980	0.1680	2.1560	0.1740
52	2.1940	0.1500	2.1500	0.1500
53	2.1820	0.1300	2.1420	0.1320

*See Figures 3b and 3c for station numbers.

Figure 3a. Vane construction details and strut coordinates (side view).

5923-3

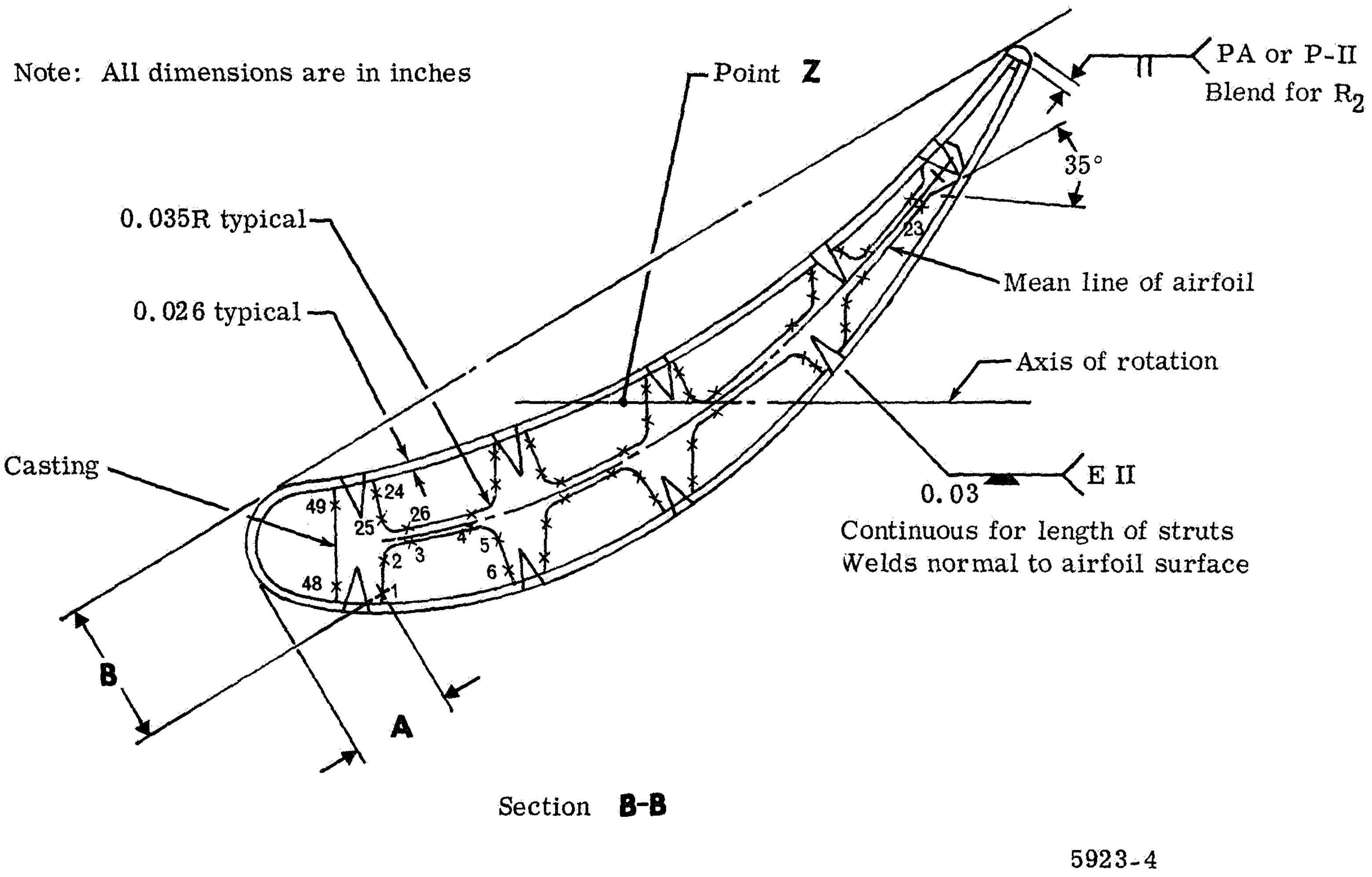

Figure 3b. Vane construction details (hub section view).

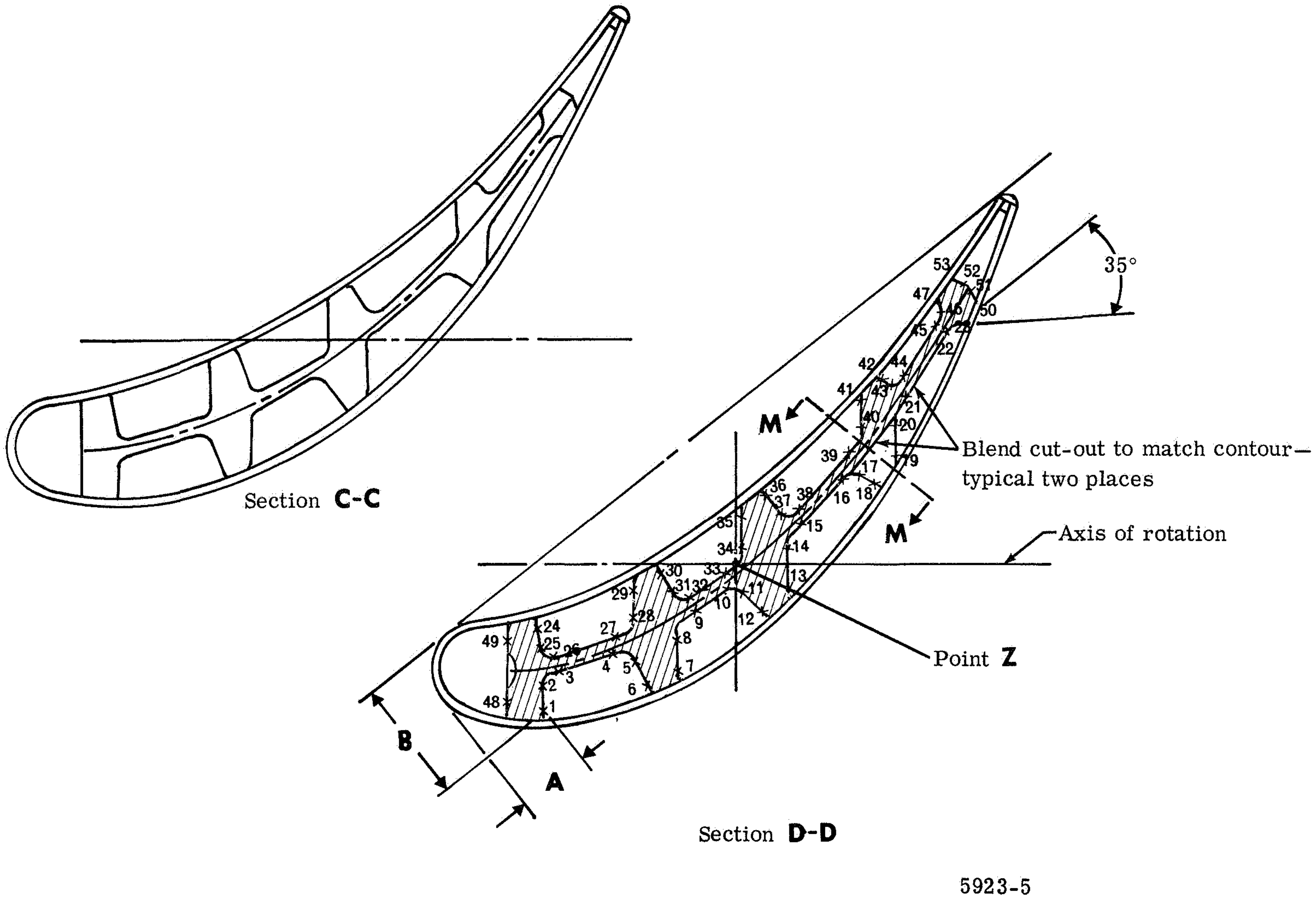

Figure 3c. Vane construction details (mean and tip section views).

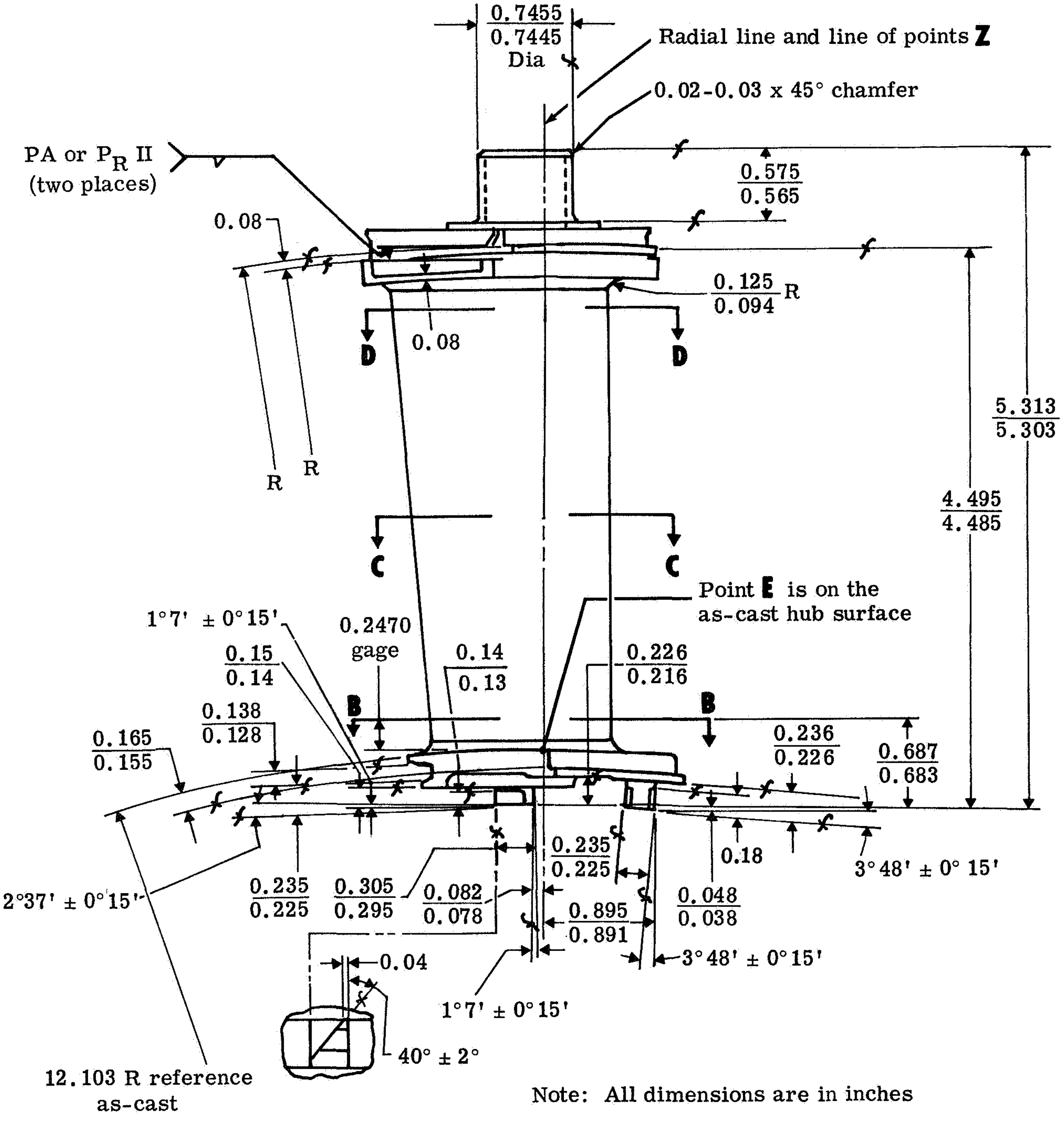

Note: All dimensions are in inches

5923-6

Figure 3d. Vane construction details (side view).

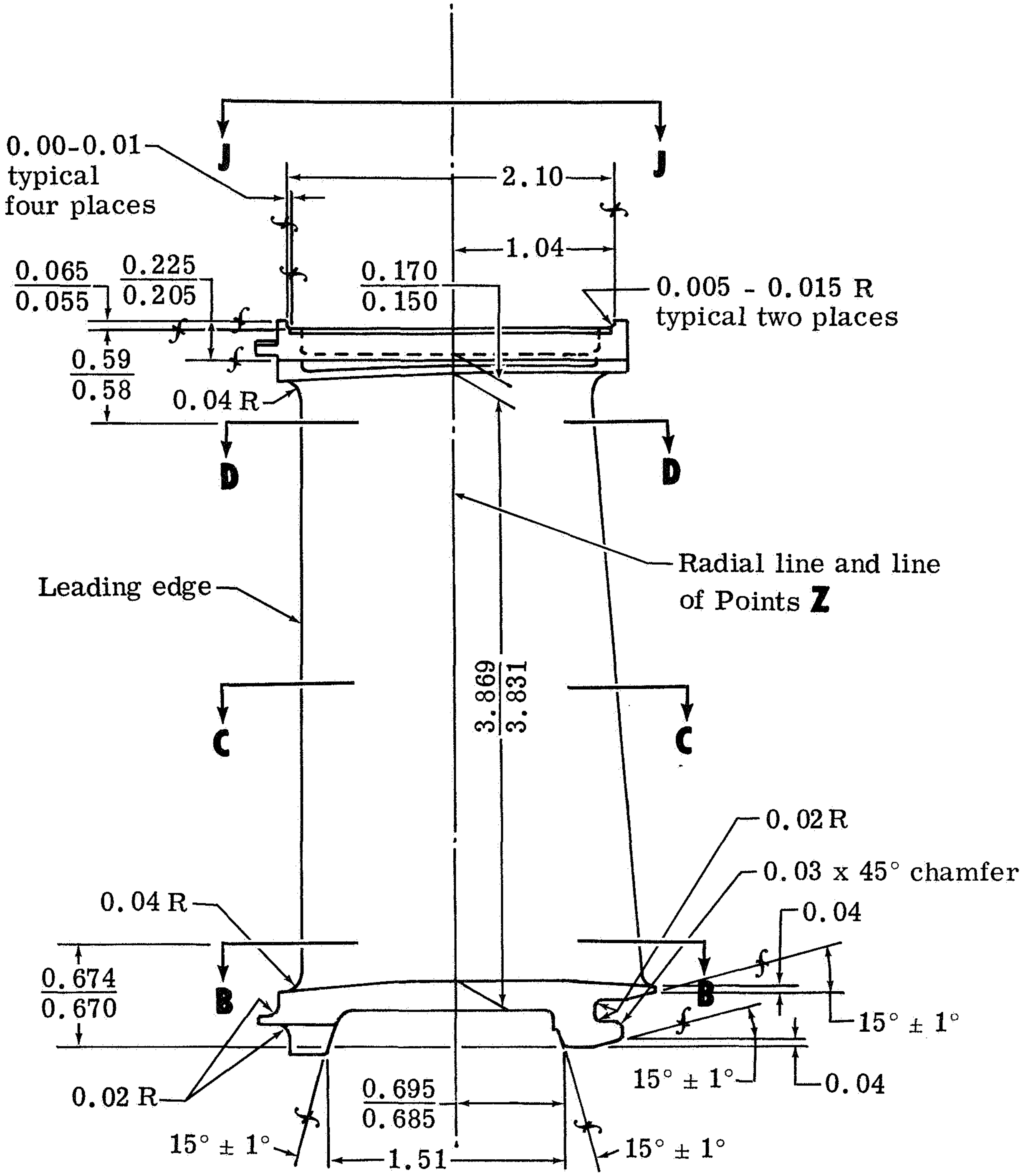

5923-7

Note: All dimensions are in inches.

Figure 3e. Vane construction details (side view).

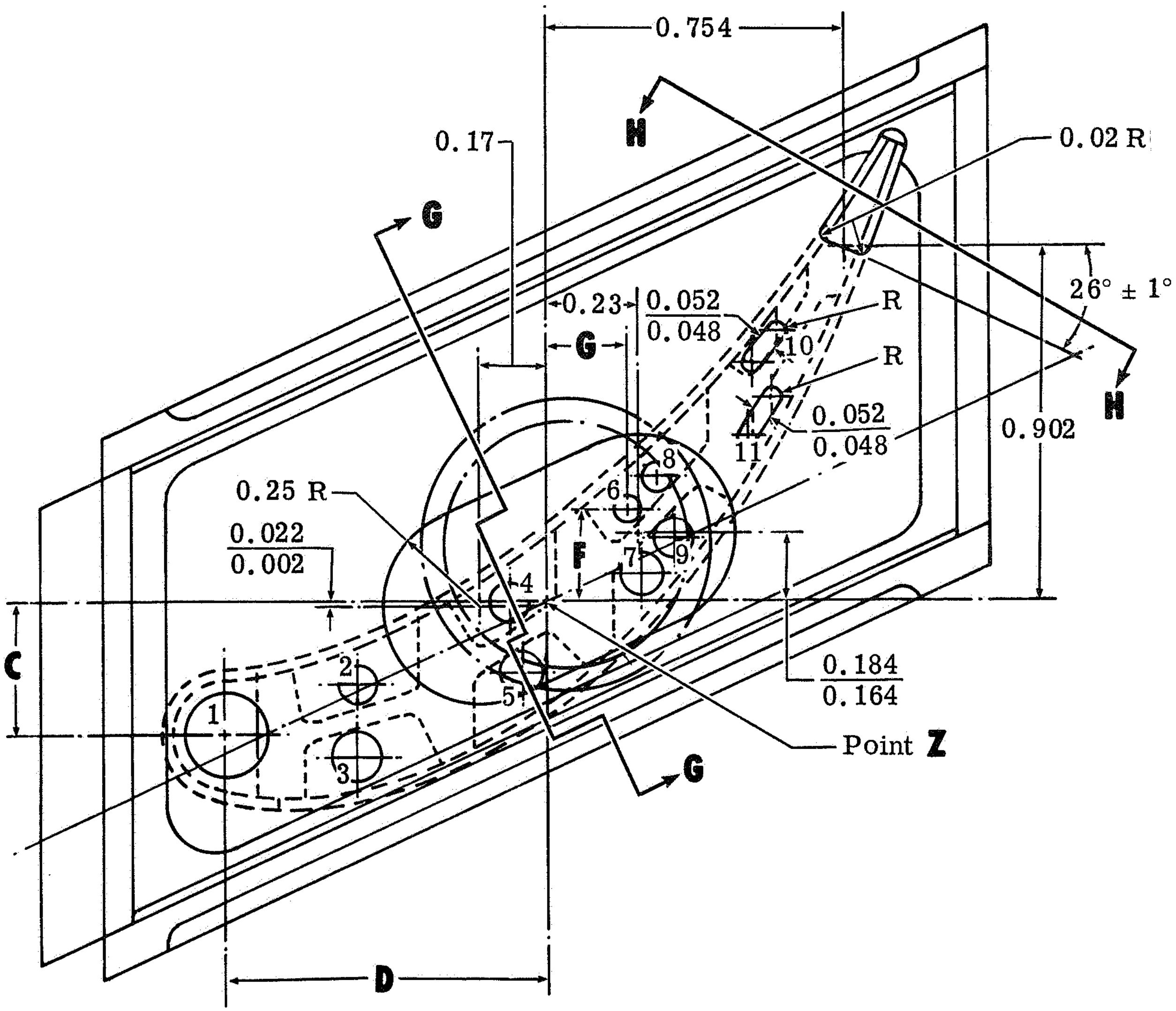

View **J-J**

Metering hole location

Hole No.	**C**	**D**	Hole dia ± 0.002
1	0.3360	0.8170	0.208
2	0.2120	0.4840	0.105
3	0.3920	0.4840	0.126
4	0.0050	0.0940	0.105
5	0.1820	0.0670	0.108

Hole No.	**F**	**G**	Hole dia ± 0.002
6	0.2340	0.2070	0.075
7	0.0740	0.2400	0.099
8	0.3140	0.2820	0.075
9	0.1600	0.3200	0.099
10	0.6110	0.5250	
	0.6880	0.5880	
11	0.4220	0.5120	
	0.5180	0.5730	

5923-8

Note: All dimensions are in inches.

Figure 3f. Vane construction details (top view).

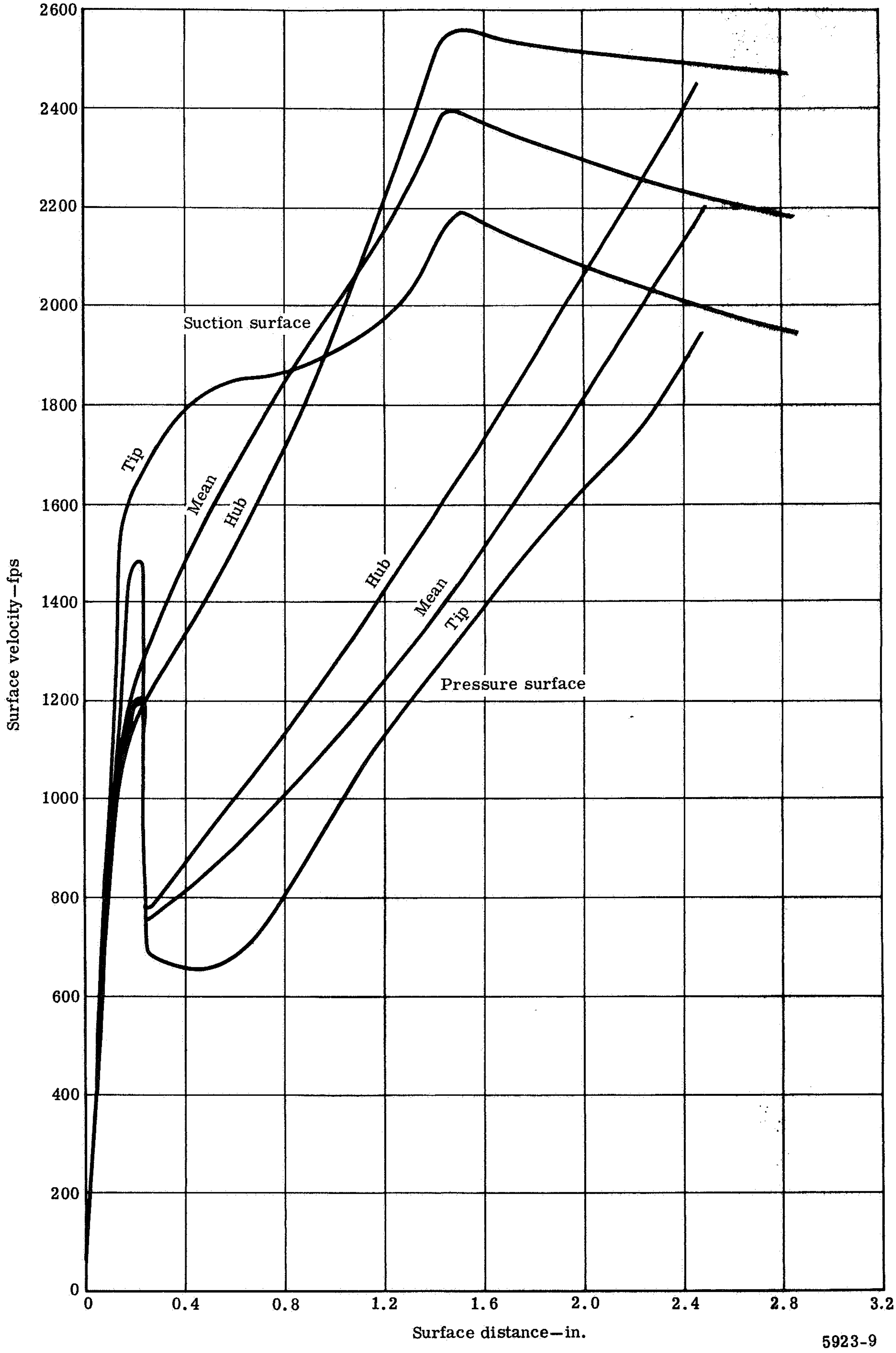

Figure 4. Gas-stream velocity distributions for the design condition.

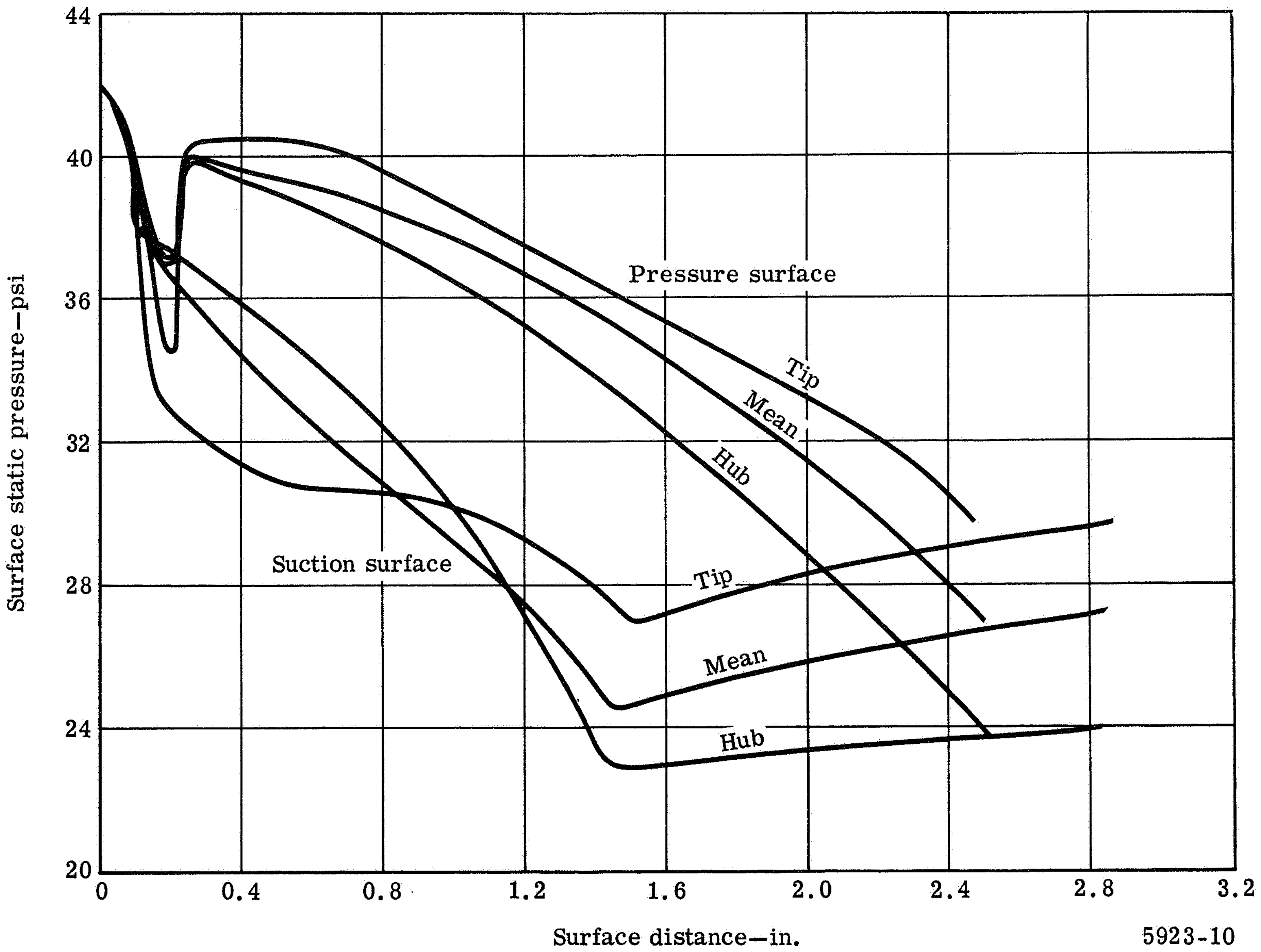

Figure 5. Gas-stream static pressure distributions for the design condition.

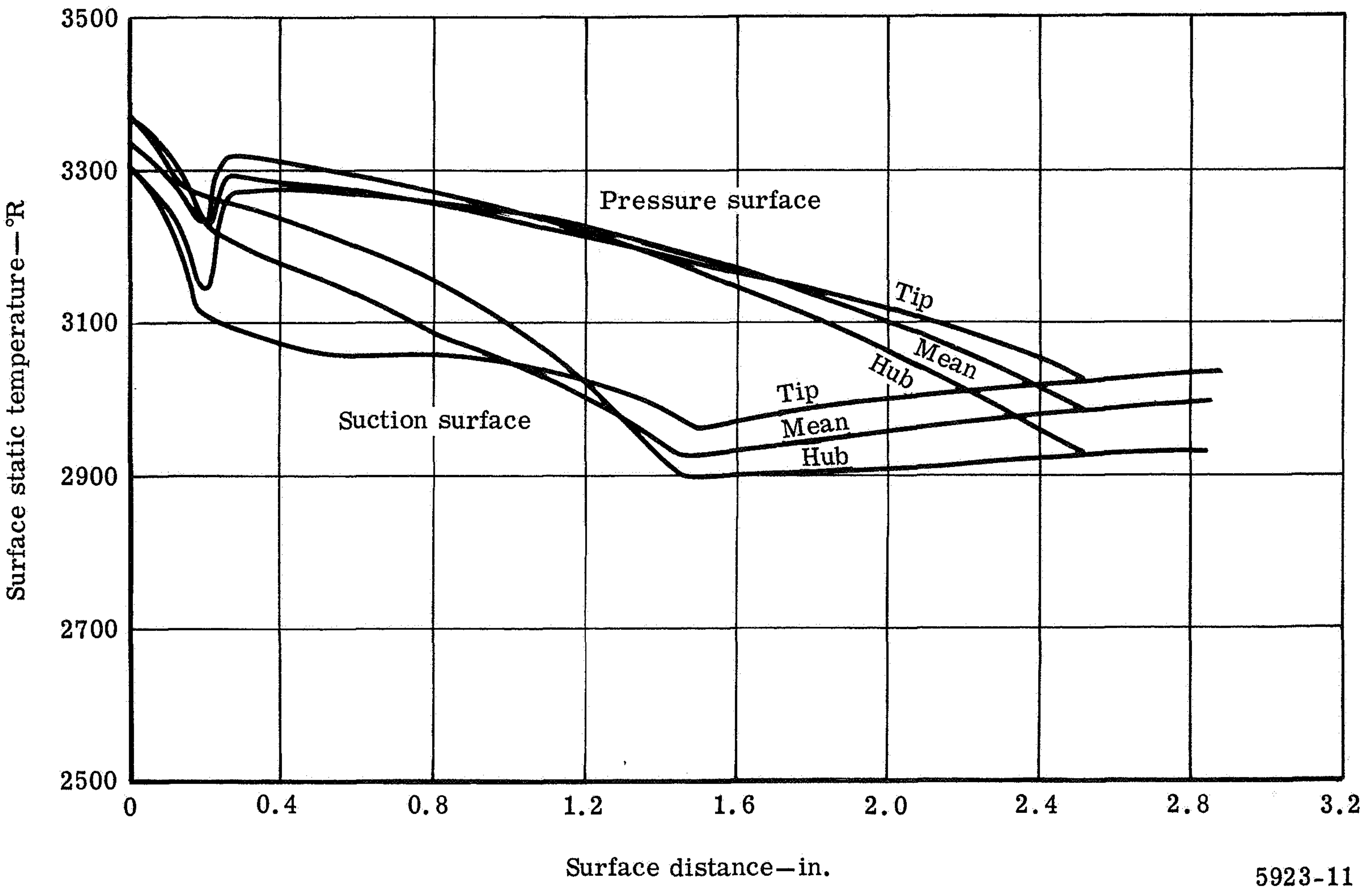

Figure 6. Gas-stream static temperature distributions for the design condition.

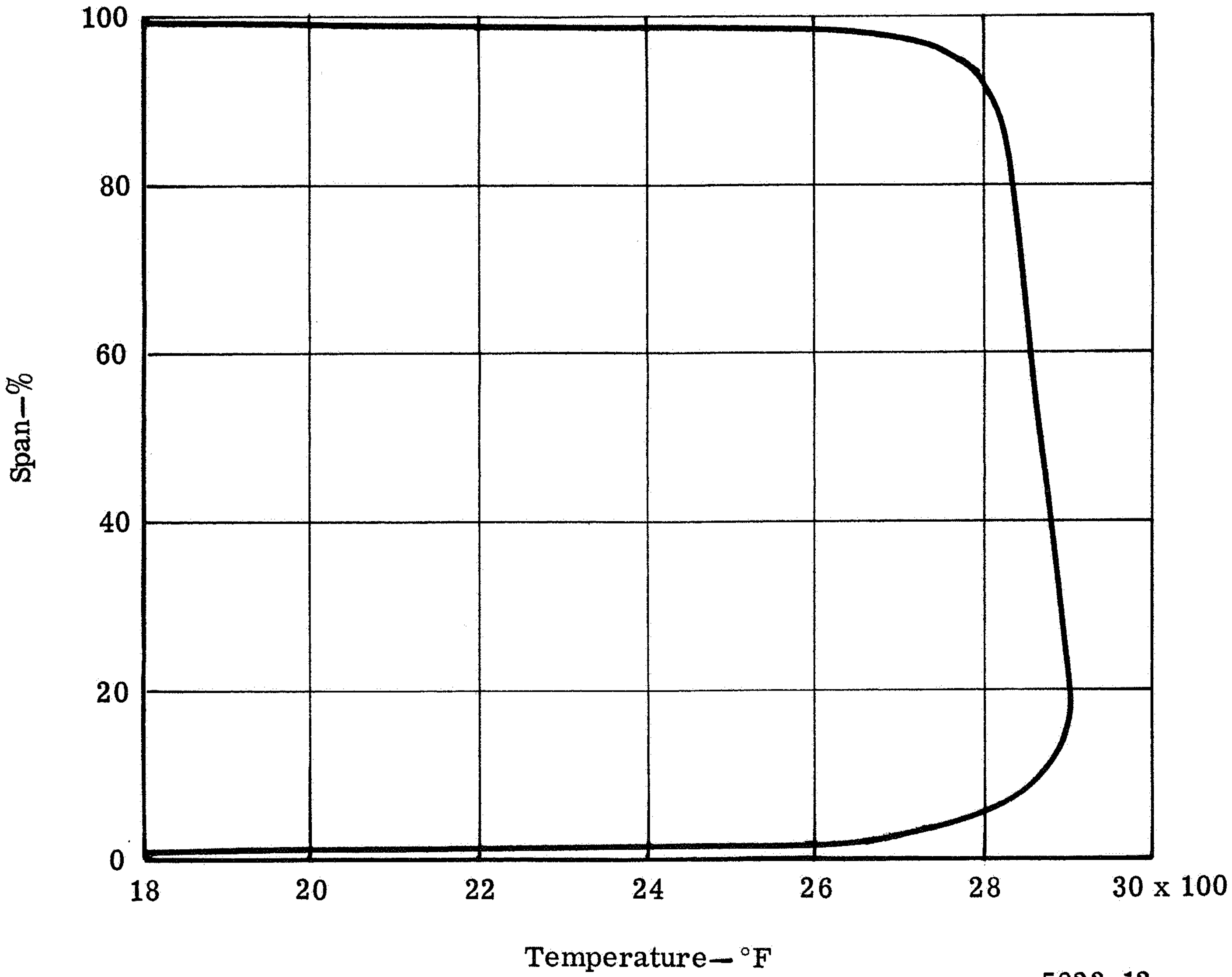

Figure 7. Gas-stream temperature distribution at stator inlet.

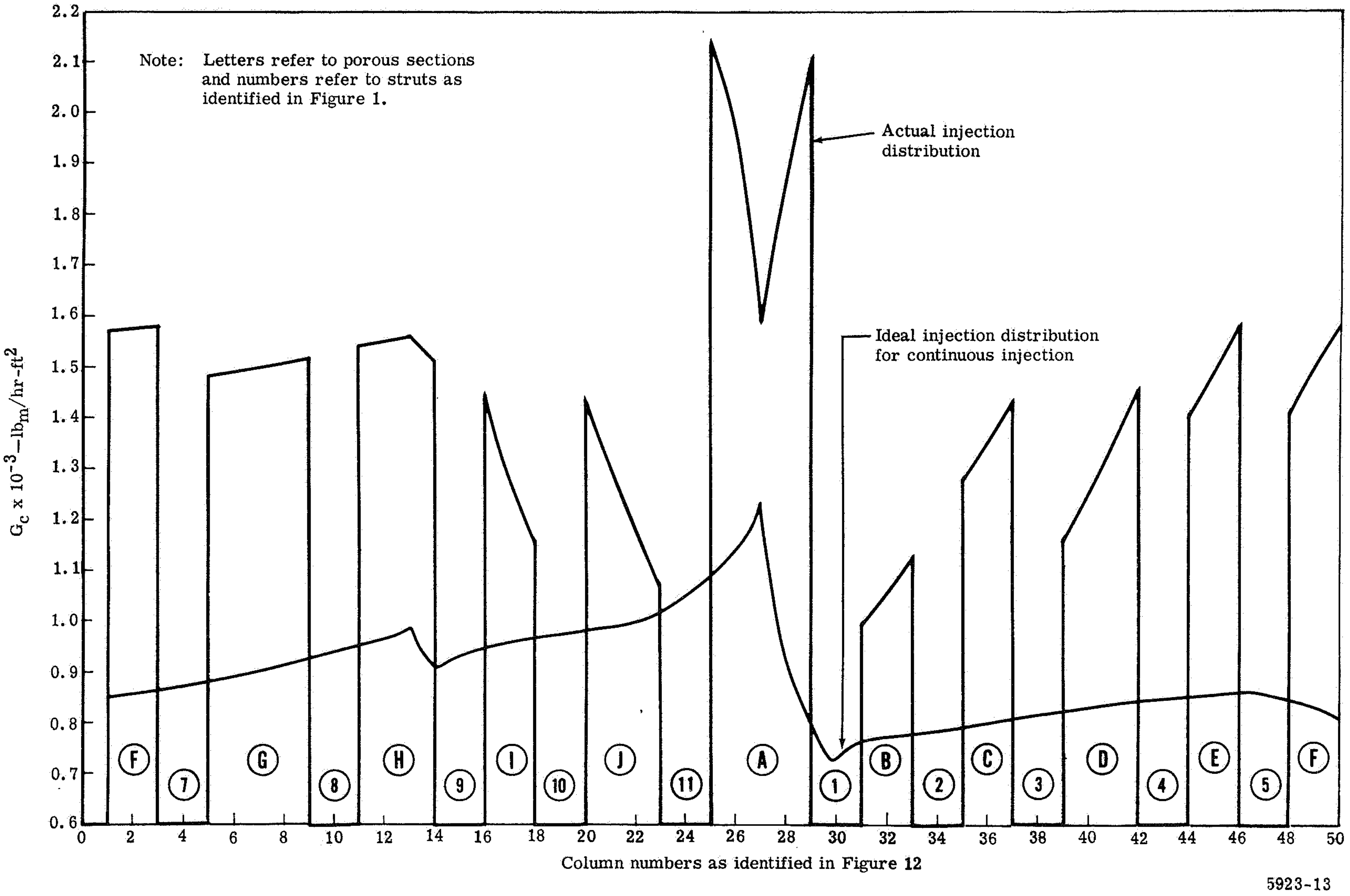

Note: Letters refer to porous sections and numbers refer to struts as identified in Figure 1.

Figure 8a. Comparison of actual and ideal blowing distributions for hub section at the design condition.

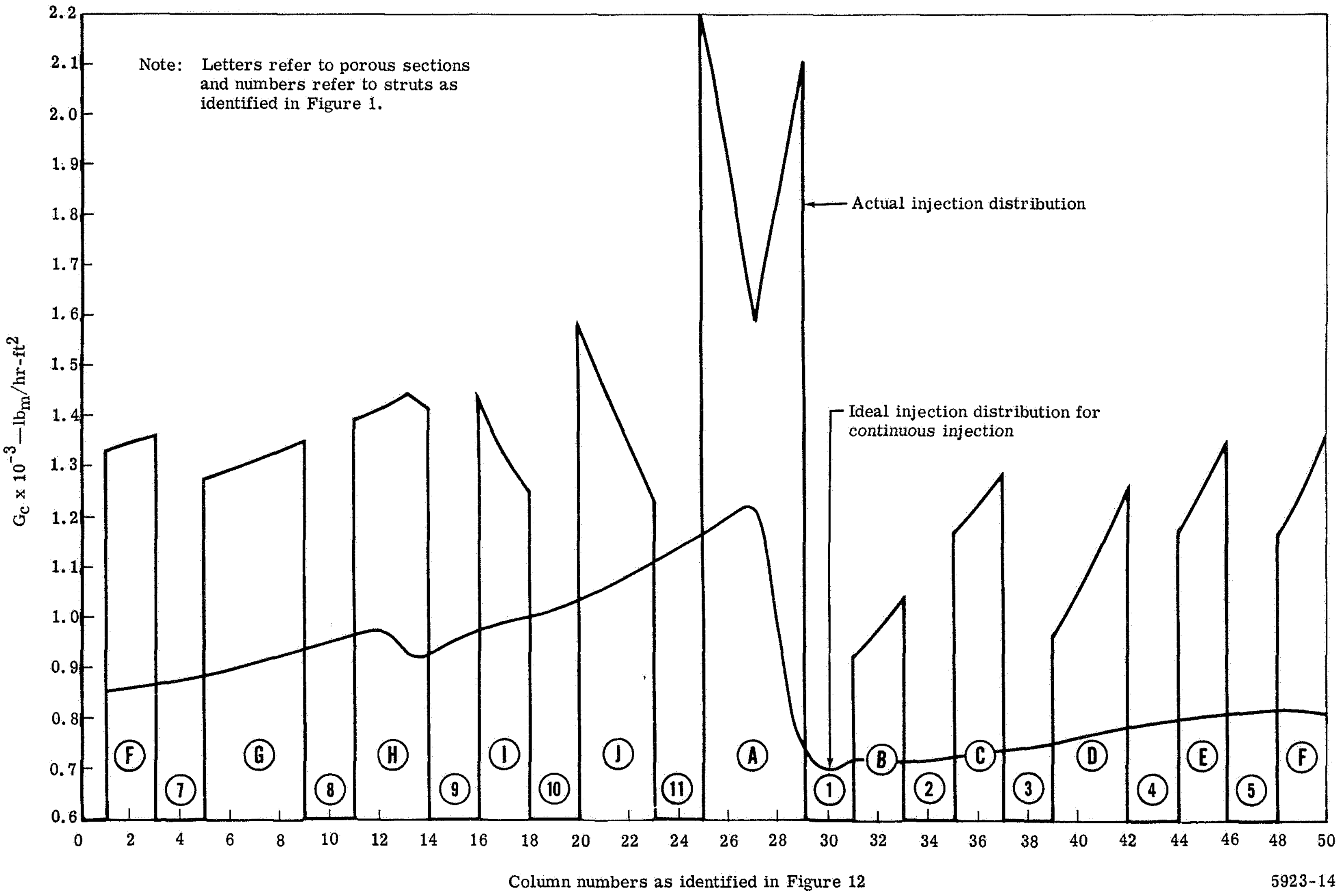

Figure 8b. Comparison of actual and ideal blowing distributions for mean section at the design condition.

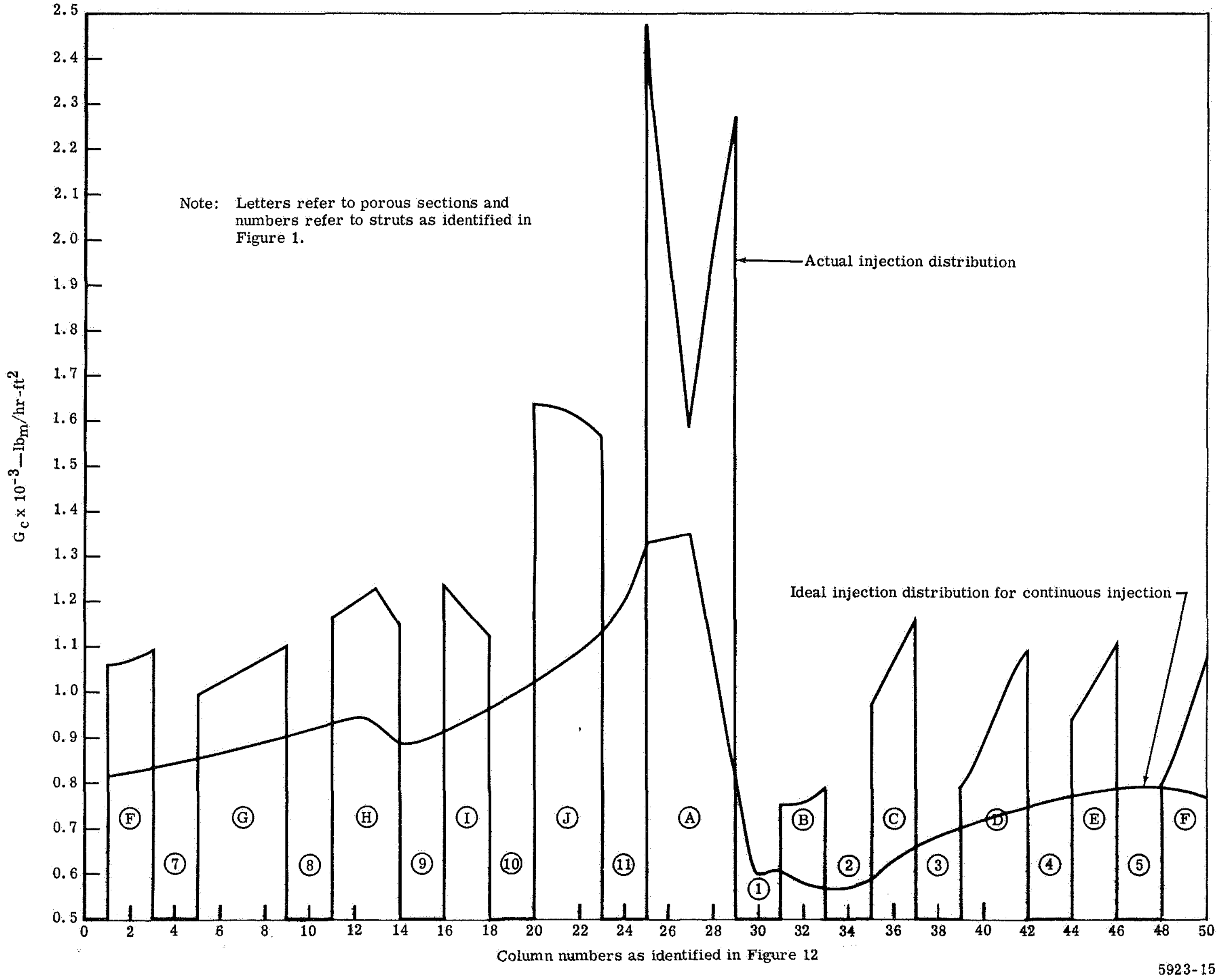

Figure 8c. Comparison of actual and ideal blowing distributions for tip section at the design condition.

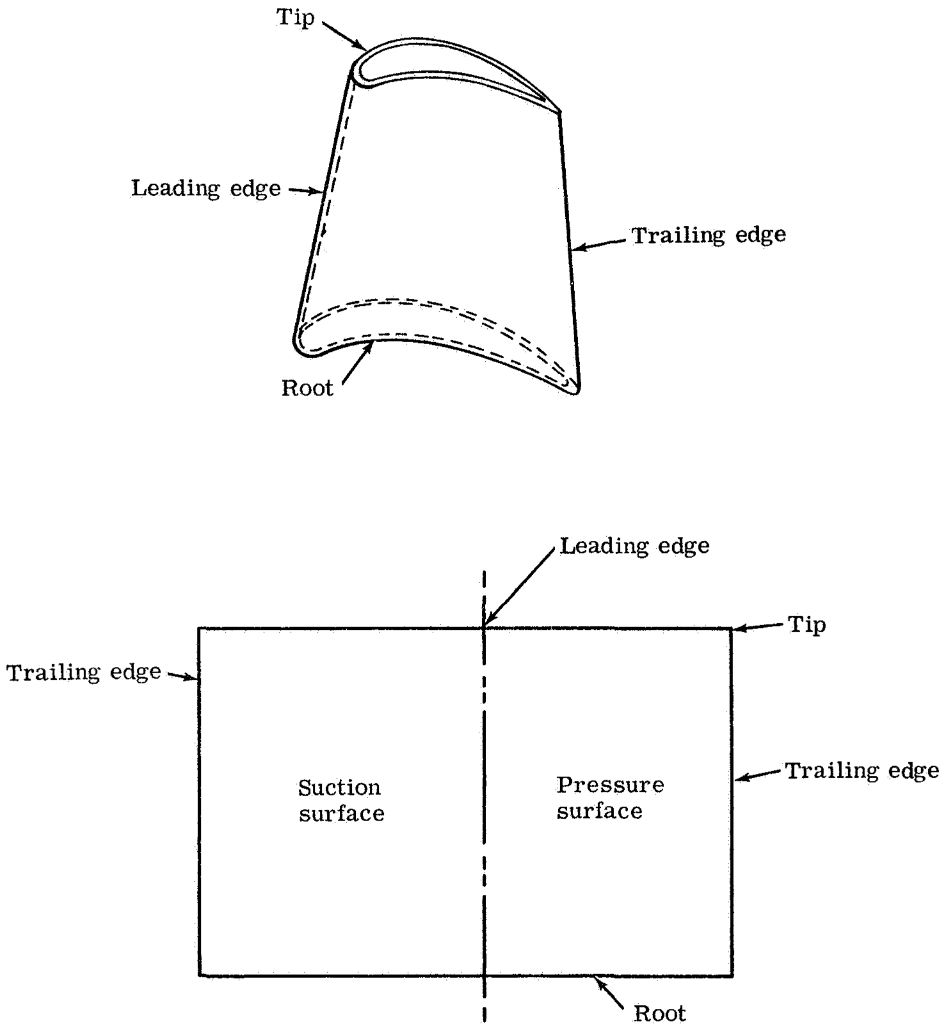

Figure 9. Schematic diagram of unfolded airfoil.

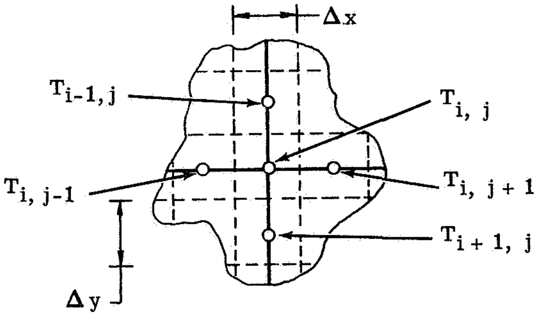

Figure 10. Typical node pattern.

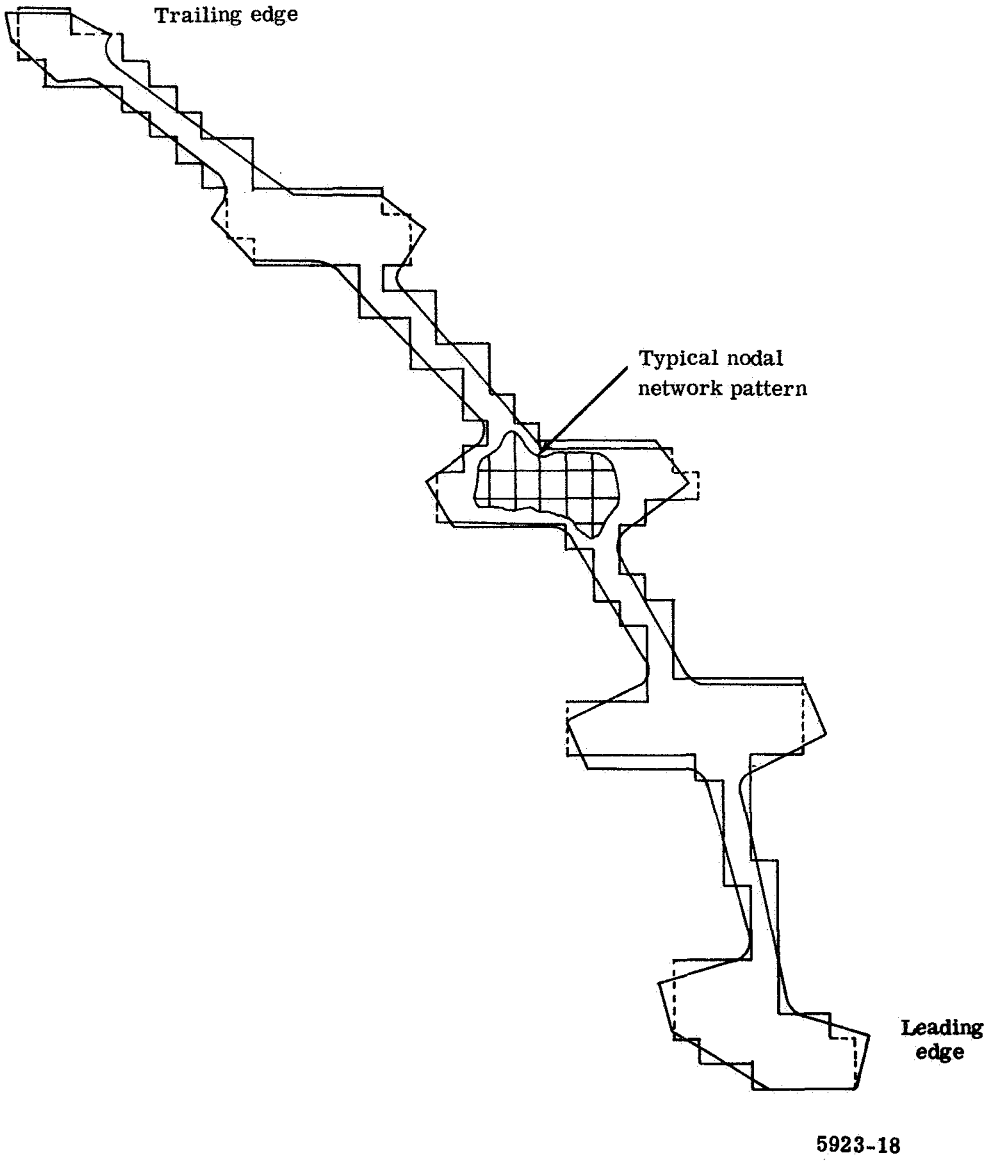

Figure 11. Strut simulation for numerical conduction analysis.

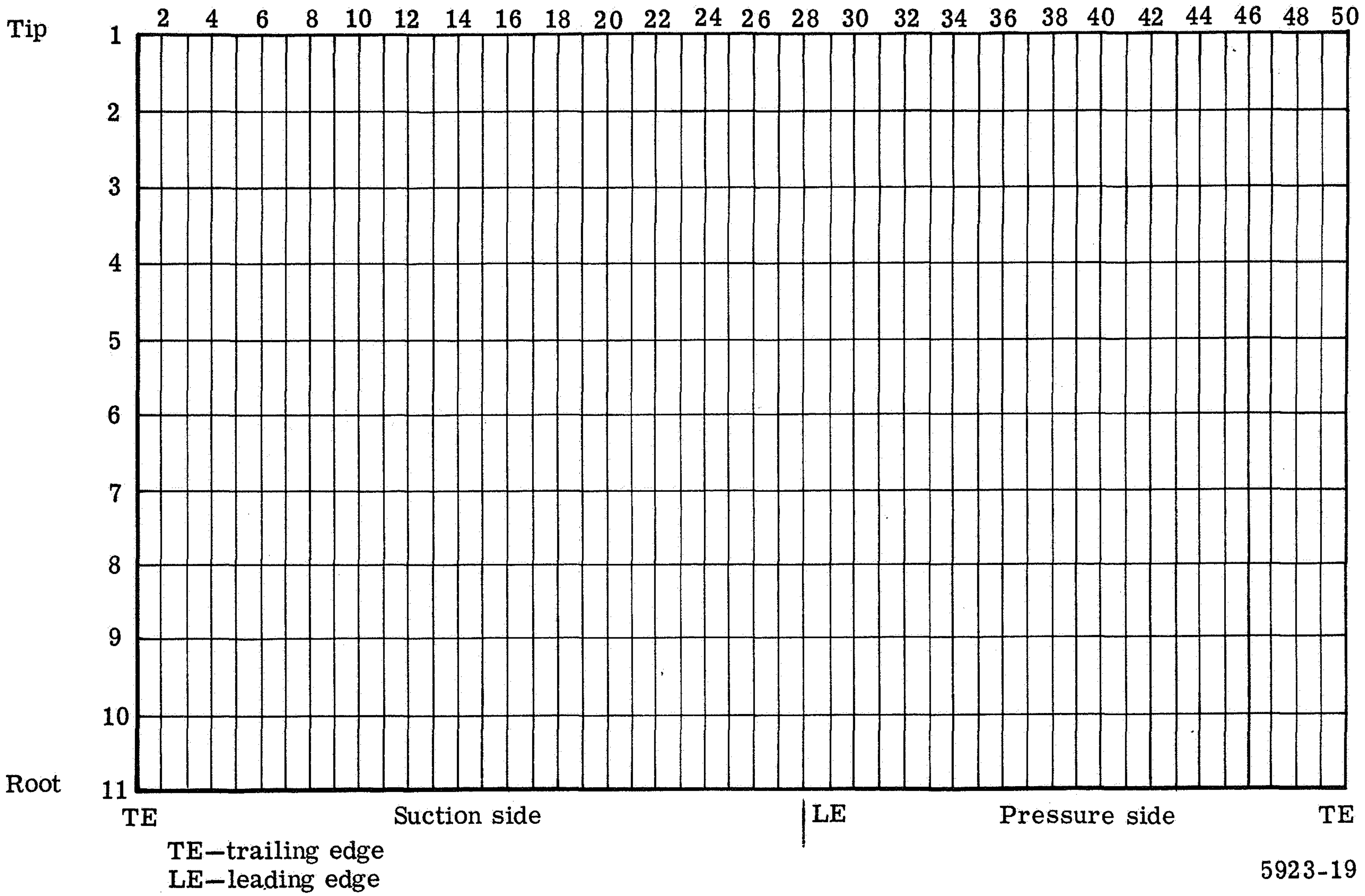

Figure 12. Nodal network for Poroloy skin thermal analysis.

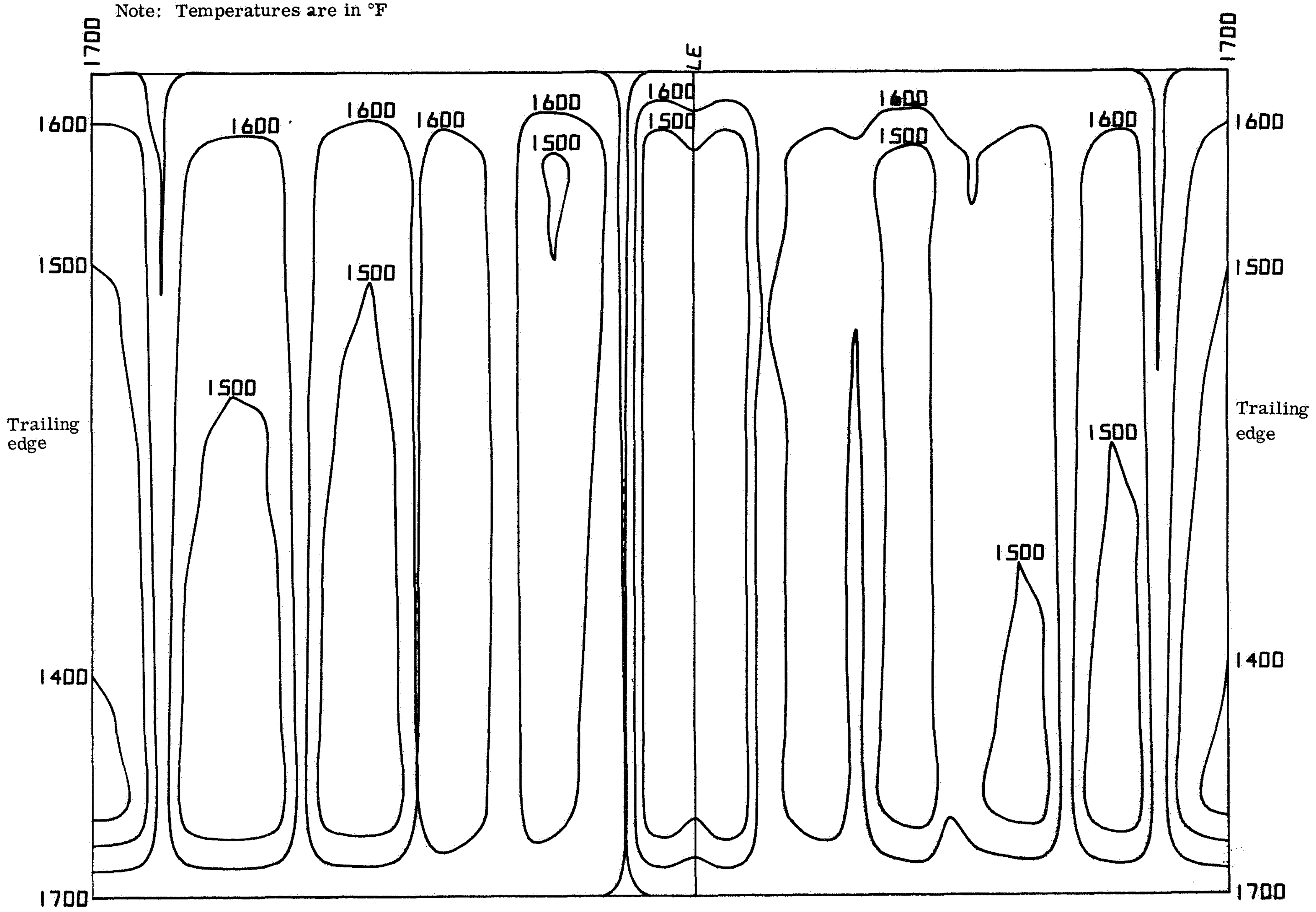

Note: Temperatures are in °F

5923-20

Figure 13. Poroloy vane isotherm map for the design condition.

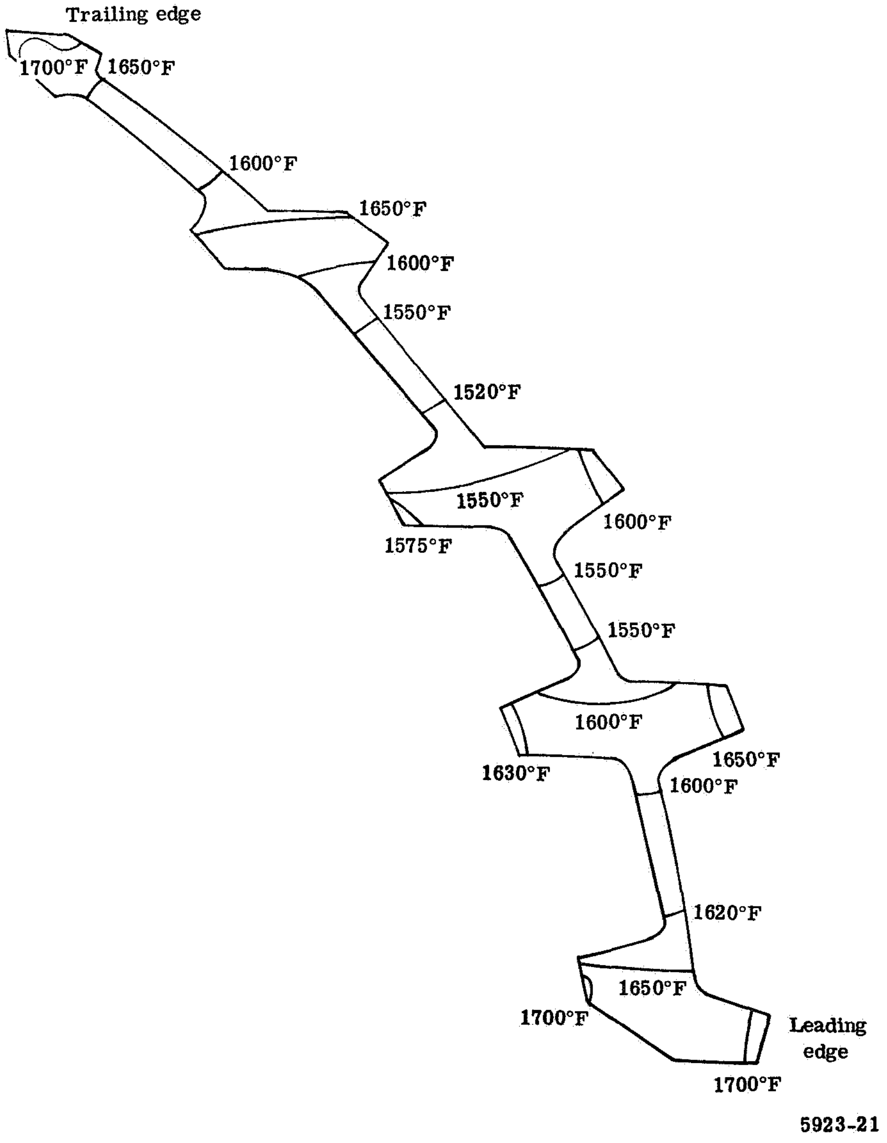

Figure 14. Isotherm pattern for strut meanline section at the design condition.

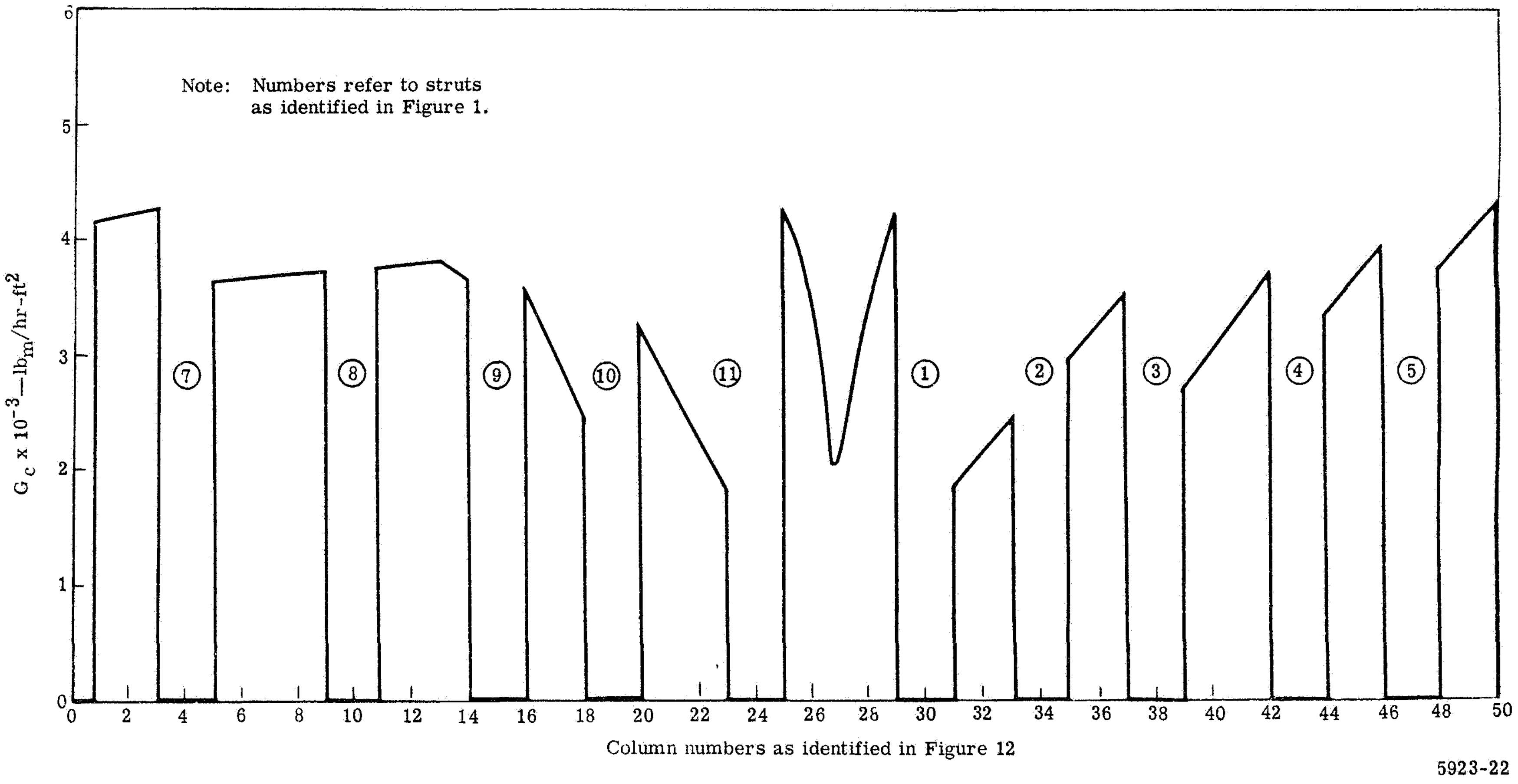

Figure 15a. Predicted blowing distribution for hub section at the off-design condition.

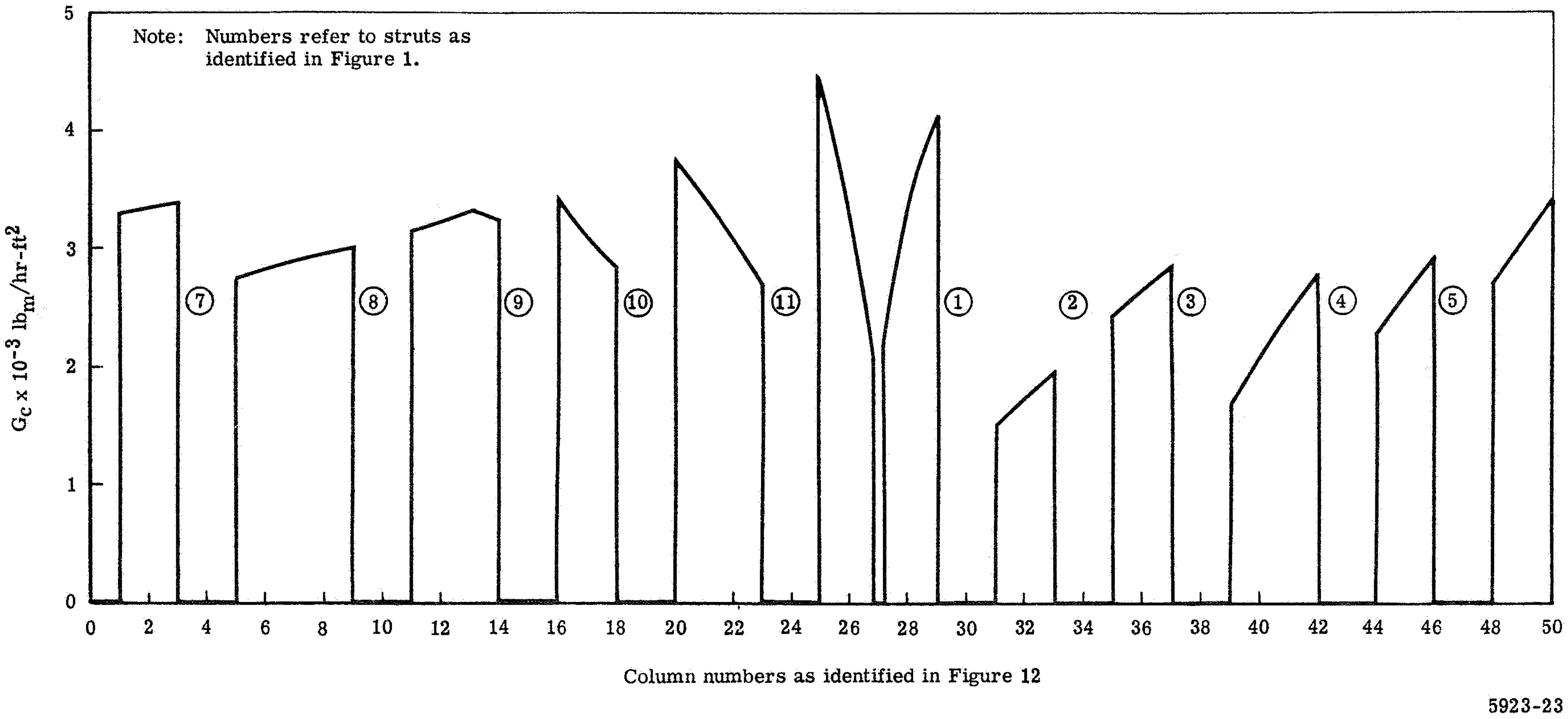

Figure 15b. Predicted blowing distribution for mean section at the off-design condition.

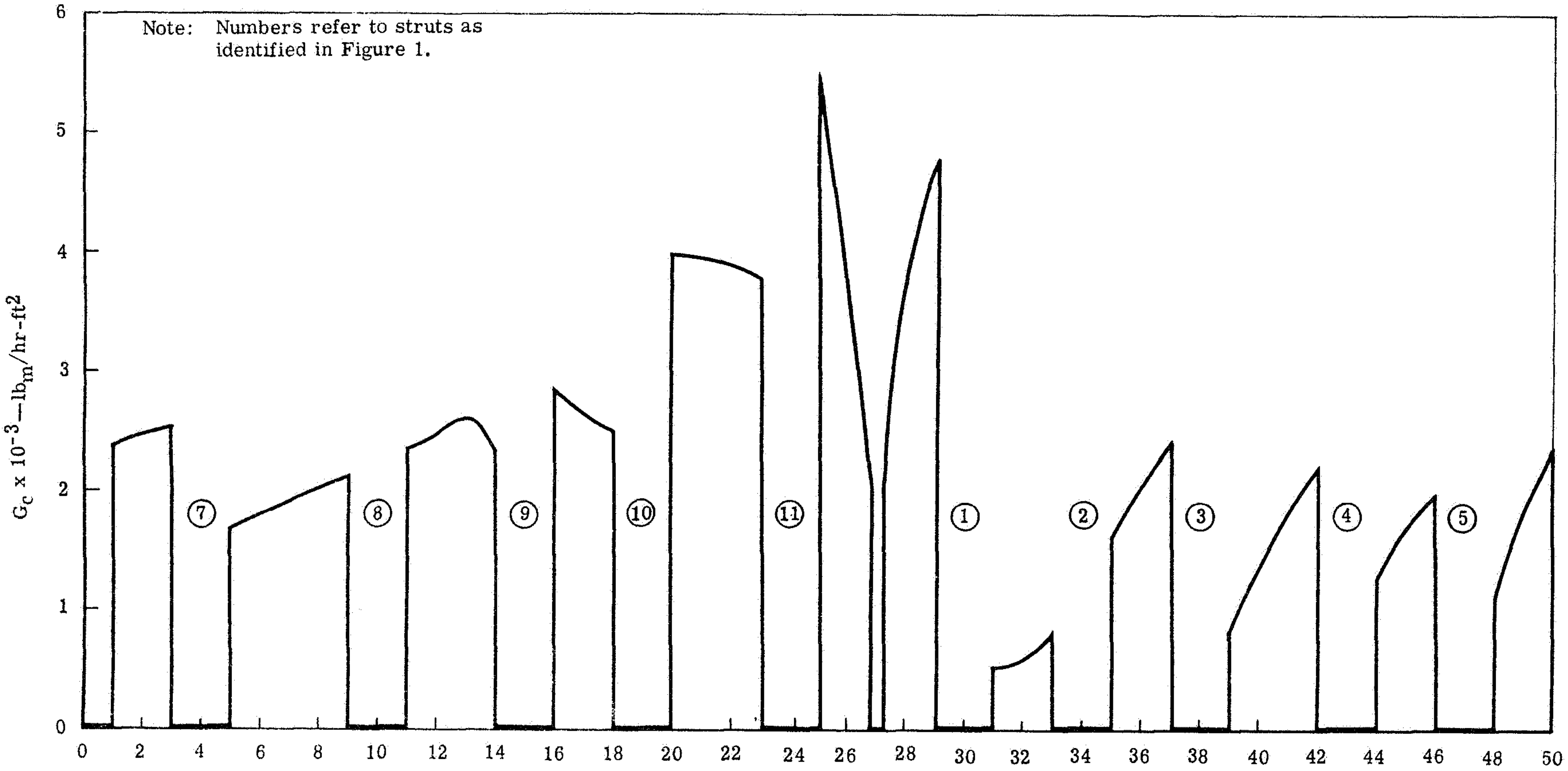

Column numbers as identified in Figure 12

5923-24

Figure 15c. Predicted blowing distribution for tip section at the off-design condition.

Note: Temperatures are in °F

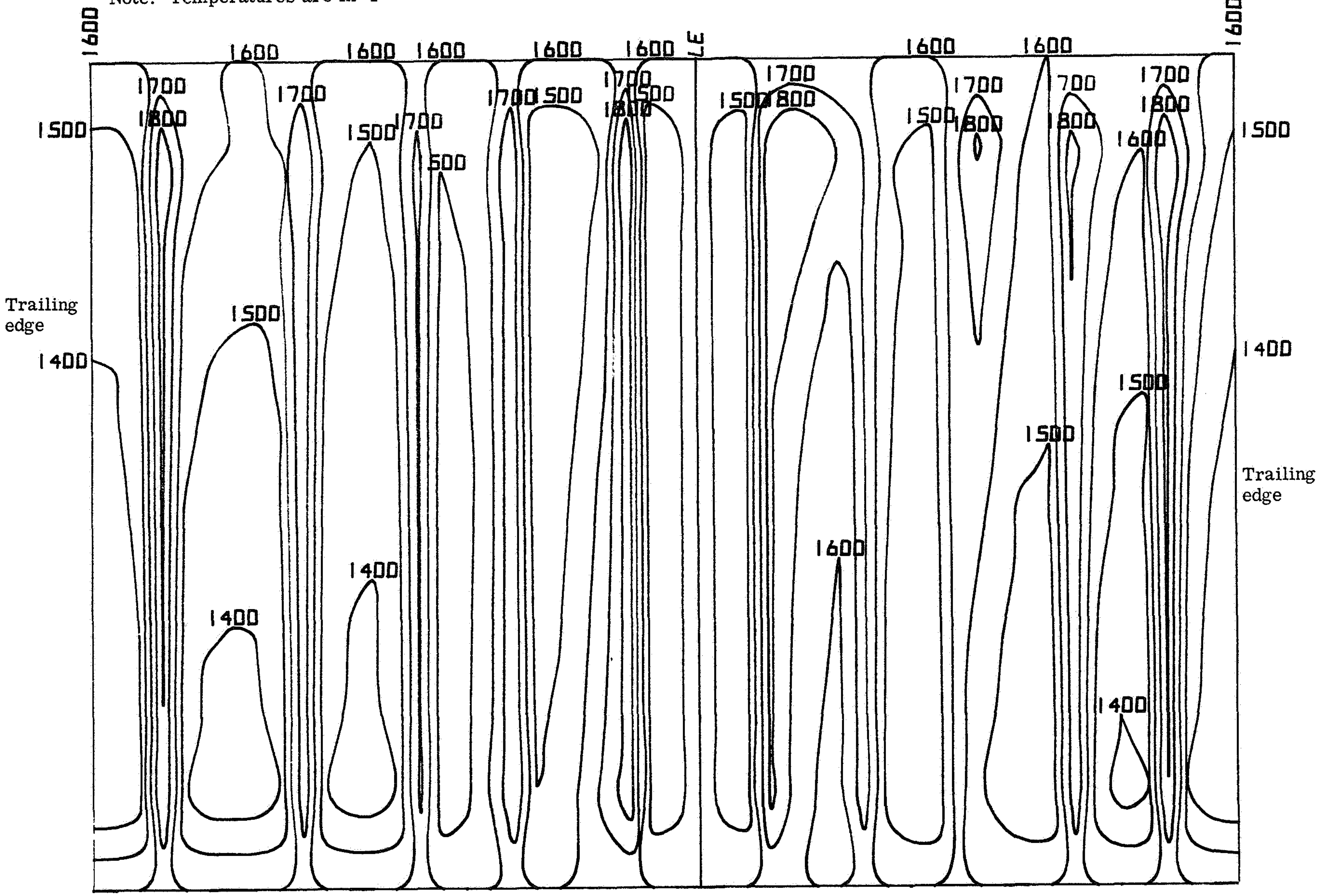

5923-25

Figure 16. Poroloy vane isotherm map for off-design condition.

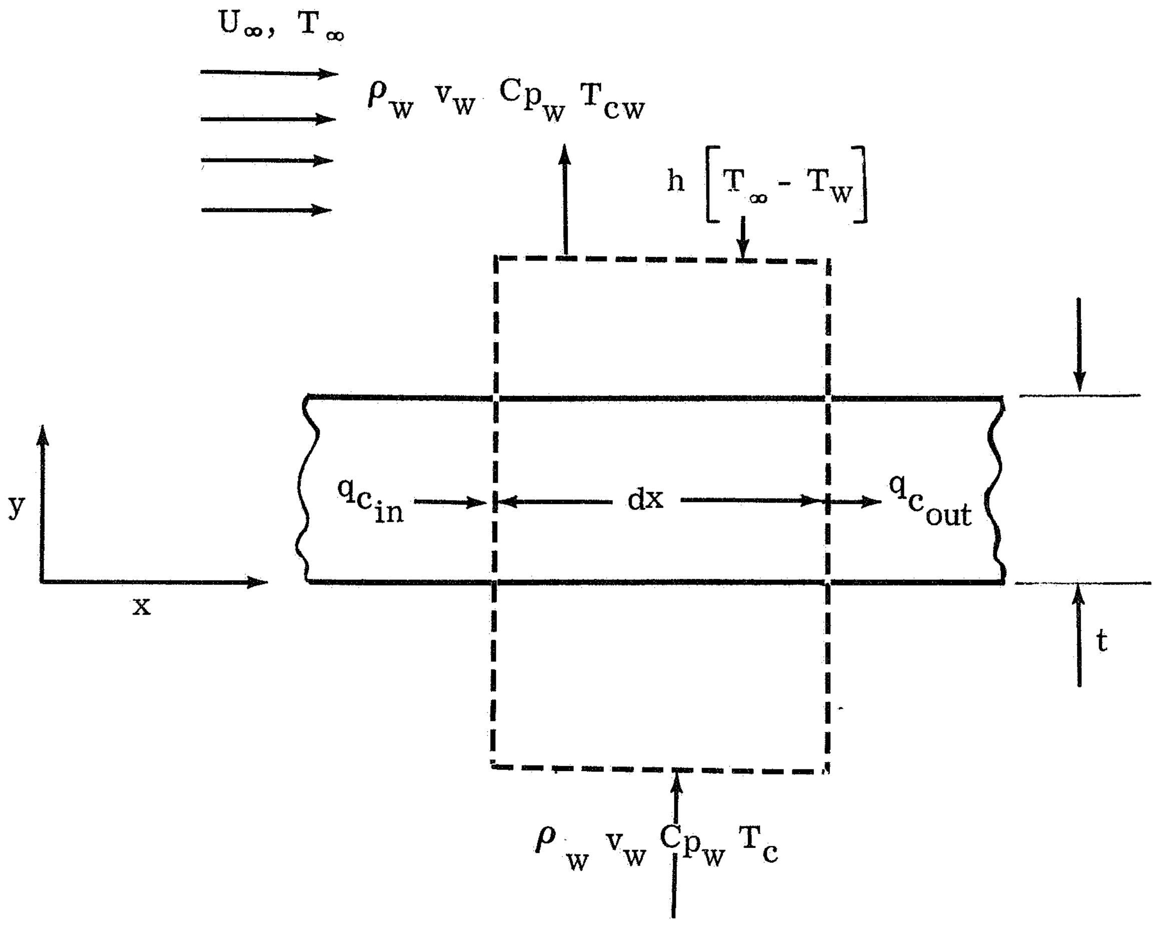

5923-26

Figure 17. Basic physical model.

DISTRIBUTION LIST

Addressee			No. of copies
NASA-Lewis Research Center			
21000 Brookpark Road			
Cleveland, Ohio 44135			
Attention:	Report Control Office	MS 5-5	1
	Technology Utilization Office	MS 3-19	1
	Library	MS 60-3	2
	Fluid System Components Div.	MS 5-3	1
	W. L. Stewart	MS 77-2	1
	J. Howard Childs	MS 60-4	1
	John H. De Ford	MS 77-3	2
	Dr. E. L. Warren	MS 60-6	15
	J. B. Esgar	MS 60-5	1
	R. H. Kemp	MS 49-1	1
	F. S. Stepka	MS 60-6	1
	R. O. Hickel	MS 60-6	1
	Dr. D. Spera	MS 49-1	1
	H. H. Ellerbrock	MS 60-4	1
	L. E. Macioce	MS 60-6	1
	Dr. J. Livingood	MS 60-6	1
	J. Lucas	MS 6-1	1
	S. Lieblein	MS 100-1	1
NASA Scientific & Technical Information Facility			
P. O. Box 33			
College Park, Maryland 20740			
Attention:	NASA Representative RQT-2448		6
FAA Headquarters			
800 Independence Avenue, SW			
Washington, D.C. 20553			
Attention:	Brig. General J. C. Maxwell		1
	F. B. Howard/SS120		1
NASA Headquarters			
600 Independence Avenue, SW			
Washington, D.C. 20546			
Attention:	N. F. Rekos (RAP)		1

Addressee	No. of copies
Department of the Army U. S. Army Aviation Material Laboratory Fort Eustis, Virginia 23604 Attention: John White	1
AFAPL (APTC) Wright-Patterson AFB, Ohio 45433 Attention: Mr. J. Richens	1
Dr. A. Wennerstrom (ARF)	1
Air Force Office of Scientific Research Propulsion Research Division USAF Washington, D. C. 20025	1
Department of The Navy Bureau of Naval Weapons Washington, D. C. 20025 Attention: Robert Brown, RAPP14	1
Department of The Navy Bureau of Ships Washington, D. C. 20360 Attention: G. L. Graves	1
NASA-Langley Research Center Langley Station Technical Library Hampton, Virginia 23365 Attention: Mark R. Nichols	1
John V. Becker	1
United Aircraft Corporation Pratt & Whitney Aircraft Division Florida Research & Development Center P. O. Box 2691 West Palm Beach, Florida 33402 Attention: R. A. Schmidtke	1

Addressee	No. of copies
United Aircraft Corporation Pratt & Whitney Aircraft Division 400 Main Street East Hartford, Connecticut 06108 Attention: G. Andreini	1
Library	1
United Aircraft Research Laboratories 400 Main Street East Hartford, Connecticut 06108 Attention: Library	1
Northern Research & Engineering Corp. 219 Vassar Street Cambridge, Massachusetts 02139 Attention: K. Ginwala	1
General Electric Co. - Flight Propulsion Division 900-1000 Western Avenue West Lynn, Massachusetts 01905 Attention: Dr. C. W. Smith - Library Bldg. 2-40M	1
Curtiss-Wright Corporation Wright Aeronautical Division Wood-Ridge, New Jersey 07075 Attention: S. Lombardo	1
G. Provenzale	1
Air Research Manufacturing Co. The Garrett Corporation, Arizona Division 402 South 36th Street Phoenix, Arizona 85934 Attention: Robert O. Bullock	1
Air Research Manufacturing Co. The Garrett Corporation 9851 Sepulveda Boulevard Los Angeles, California	1

Addressee No. of copies

AVCO Corporation
Lycoming Division
550 South Main Street
Stratford, Connecticut 06497
Attention: C. W. Bolton 1
Charles Kuintzel 1

Continental Aviation & Engineering Corporation
12700 Kercheval Avenue
Detroit, Michigan 48215
Attention: Eli H. Benstein 1
Howard C. Welch 1

International Harvester Company, Solar
2200 Pacific Highway
San Diego, California 92112
Attention: P. A. Pitt 1
Mrs. L. Walper 1

Goodyear Atomic Corporation
Box 268
Piketon, Ohio 45661
Attention: Department No. 423 for C. O. Longebrake 1

George Derderian AIR 53622B
Department of The Navy
Bureau of Navy
Washington, D.C. 20360 1

The Boeing Company
Commercial Airplane Division
P. O. Box 3707
Seattle, Washington 98124
Attention: G. J. Schott, M.S. 80-66 1

The Boeing Company
Missile and Information Systems Division
224 N. Wilkinson Street
Dayton, Ohio 45402
Attention: Warren K. Thorson 1

Addressee	No. of copies
Wall Colmonoy Corporation 19345 John R. Street Detroit, Michigan Attention: R. L. Peaslee	1
Aerojet-General Corporation P. O. Box 1947 Sacramento, California 95899 Attention: M. S. Nylin	1
Library	1
The Bendix Corporation Research Laboratories Division 20900 - 10 1/2 Mile Road Southfield, Michigan 48076 Attention: A. R. Spencer	1
Battelle Memorial Institute 505 King Avenue Columbus, Ohio 43201 Attention: Defense Metals Information Center Attention: Robert T. Niehoff	1
Bendix Filter Division 434 West 12 Mile Road Madison Heights, Michigan 48071 Attention: A. G. McLemore	1
F. W. Cole	1
Air Force Materials Laboratory Wright-Patterson Air Force Base, Ohio 45433 Attention: MAAM, Mr. Hughes	1
MAMP, Mr. Hendricks	1
Douglas Aircraft Company 3855 Lakewood Blvd. Long Beach, California 90801 Attention: Technical Information Center, CL-250 for J. E. Merriman	1

Addressee	No. of copies
Engineering Library	
TRW Inc.	
23555 Euclid Avenue	
Cleveland, Ohio 44117	
Attention: Elizabeth Barrett, Librarian	1
J. Edward Taylor, Director Product Development	
Jet and Ordnance Division	1
Westinghouse Electric Corporation	
Small Steam and Gas Turbine Engineering B-4	
Lester Branch	
P. O. Box 9175	
Philadelphia, Pennsylvania 19113	
Attention: S. M. De Corso	1
J. J. Watt	1